UNIVERSITY OF CALIFORNIA, SAN DIEGO

Internal structure of metallic nanocrystals using coherent x-ray imaging

A dissertation submitted in partial satisfaction of the
requirements for the degree
Doctor of Philosophy

in

Materials Science and Engineering

by

Jong Woo Kim

Committee in charge:

Professor Oleg Shpyrko, Chair
Professor Sungho Jin, Co-Chair
Professor Renkun Chen
Professor Ying Shirley Meng
Professor Sunil Sinha

2015

The dissertation of Jong Woo Kim is approved, and it is acceptable in quality and form for publication on microfilm and electronically:

_____

_____

_____

_____
Co-Chair

_____
Chair

University of California, San Diego

2015

DEDICATION

This thesis work is dedicated to my wife, Jimin, who has been so supportive through the process of pursuing the Ph.D degree. This work is also dedicated to my father, Bongsu Kim, who loved me and always prayed for me.

TABLE OF CONTENTS

LIST OF FIGURES

LIST OF TABLES

ACKNOWLEDGEMENTS

I would like to thank my thesis advisor Prof. Oleg Shpyrko for providing great opportunities to do research and his advices on the projects that I have carried out. It is unforgettable that he encouraged and helped me continuously during my Ph.D program. I would also like to thank my co-advisor Prof. Sungho Jin for his help and advice on my research. I would like to express the deepest gratitude to my other committee members: Prof. Sunil Sinha, Prof. Shirley Meng, and Prof. Renkun Chen. Over the years, each has given me superb scientific guidance, many insightful suggestions.

Chapter 5, in full, is a reprint of the material "Curvature-induced and thermal strain in polyhedral gold nanocrystals" as it appears in the Applied Physics Letters, Jong Woo Kim, Sohini Manna, Sebastian H. Dietze, Andrew Ulvestad, Ross Harder, Edwin Fohtung, Eric E. Fullerton and Oleg G. Shpyrko, 2014, 105, 173108. The dissertation author was the primary investigator and author of this paper.

Chapter 6, in full is currently being prepared for submission for publication of the material "Observation of x-ray radiation pressure on a Ni nanowire". Jong Woo Kim, Edwin Fohtung, Sohini Manna, Ross Harder, Andrej Singer, Leandra Boucheron, Eric E. Fullerton, Oleg G. Shpyrko. The dissertation author was the primary investigator and author of this paper.

I would like to acknowledge the financial support from US Department of Energy, Office of Science, Office of Basic Energy Sciences, under Contract DE-SC0001805 and use of the Advanced Photon Source, an Office of Science User Facility operated for the U.S. Department of Energy (DOE) Office of Science by Argonne National Laboratory, supported by the U.S. D.O.E. under Contract No. DE-AC02-06CH11357.

VITA

1998	Bachelor of Science, Seoul National University, South Korea
2004	Master of Science, Seoul National University, South Korea
2015	Doctor of Philosophy, University of California, San Diego

PUBLICATIONS

J. W. Kim, S. Manna, S. H. Dietze, A. Ulvestad, R. Harder, E. Fohtung, E. E. Fullerton and O. G. Shpyrko , "Curvature-induced and thermal strain of polyhedral gold nanocrystals", *Appl. Phys. Lett. 105, 173108* (2014)

A. Singer, A. Ulvestad, H.-M. Cho, J. W. Kim, J. Maser, R. Harder, S. Meng, and O. G. Shpyrko, "Non-equilibrium structural dynamics of nanoparticles in $LiNi_{1/2}Mn_{3/2}O_4$ cathode under operando conditions ", *Nano. Lett. 14, 5295.* (2014)

A. Ulvestad, H. M. Cho, R. Harder, J. W. Kim, S. H. Dietze, E. Fohtung, Y. S. Meng and O. G. Shpyrko, "Nanoscale Strain Mapping in Battery Nanostructures", *Appl. Phys. Lett. 104, 073108.* (2014)

E. Fohtung, J. W. Kim, Keith T. Chan, R. Harder, E. Fullerton, and O. G. Shpyrko, "Probing the three-dimensional strain inhomogeneity and equilibrium elastic properties of single crystal Ni nanowires.", *Appl. Phys. Lett. 101, 033107.* (2012)

A. Ulvestad, A. Singer, J.N. Clark, C.H. Cho, J. W. Kim, R. Harder, J. Maser, Y.S. Meng and O. G. Shpyrko , "Topological defect dynamics in operando battery nanoparticles", *Submitted*

J. W. Kim, E. Fohtung, S. Manna, R. Harder, A. Singer, L. Boucheron, E. E. Fullerton and O. G. Shpyrko, "Observation of x-ray radiation pressure on a nickel nanocrystal", *In preparation*

ABSTRACT OF THE DISSERTATION

Internal structure of metallic nanocrystals using coherent x-ray imaging

by

Jong Woo Kim

Doctor of Philosophy in Materials Science and Engineering

University of California, San Diego, 2015

Professor Oleg Shpyrko, Chair
Professor Sungho Jin, Co-Chair

Gold nanocrystals are increasingly important for a wide range of potential applications in photonics, nanoelectronics, biological imaging, and biosensors. Although various synthesis methods for Au nanocrystals have been developed, most synthesis technique employ surfactants to control shape and/or size. However, we synthesized polyhedral shaped gold nanocrystals in the absence of any foreign catalysts so that we were able to avoid any influences of surfactants on the phys-

ical properties of the nanocrystals. We then used coherent diffractive imaging to investigate the nanoscale internal structure, shape, and lattice distortion of the Au nanocrystals and understand growth dynamics and suitability of the synthesis technique.

This is the first study of both curvature-induced strain under a locally rounded surface and the effect of thermally induced lattice strain at the nanocrystal-substrate interface in a single Au nanocrystal. It is confirmed that the strain distribution on the locally curved surface of the Au nanoparticle is consistent with the theoretical prediction known as the Young-Laplace effect. In contrast, the strain at the interface with the substrate is anomalous. We attribute it to the dissimilar interfacial energies between Au/Air and Au/Si and to the difference in thermal expansion between the nanocrystal and the substrate during the cooling process. These results indicate that the lattice strain of nanocrystals is influenced both by their interactions with the substrate as well as the geometric details.

Chapter 1

Introduction

Gold nanocrystals are attracting increasing interest within the scientific community due to the inherent differences between their optical and electronic properties and those of their bulk counterparts. Gold nanocrystals are important for a wide range of potential applications in photonics, nanoelectronics, biological imaging, and biosensors [1, 2, 3, 4]. Although various synthesis methods for Au nanocrystals have been developed, most synthesis technique employ surfactants to control shape and/or size. However, we synthesized polyhedral shaped gold nanocrystals in the absence of any foreign catalysts so that we were able to avoid any influences of surfactants on the physical properties of the nanocrystals.

We then used coherent diffractive imaging to investigate the nanoscale internal structure, shape, and lattice distortion of the Au nanocrystals and understand growth dynamics and suitability of the synthesis technique. Coherent x-ray diffractive imaging is a technique that probes not only the overall shape of a nanocrystal,

but also the displacement of individual atoms because coherent x-ray diffraction is highly sensitive to internal strains within a crystal, which appear as a change of phase in the complex image [5, 6, 7, 8, 9, 10]. A coherent x-ray diffraction pattern can be inverted to a complex-valued density function. The amplitude of this complex function is proportional to the electron density in the crystal, and the phase corresponds to the displacement of the lattice as projected onto the momentum transfer vector, which is determined by the direction of incident and scattered x-ray, of the Bragg peak. This non-destructive way of probing internal 3D properties of single nanocrystals allows us to investigate strain of objects in the as-prepared state. In principle, more than three independent momentum transfer vectors have allowed a full mapping of the strain tensor within a nanocrystal [11]. This technique has been used to explore interdisciplinary science, including metallic nanostructures, strain evolution of a single nanoparticle in a LNMO cathode during charging/uncharging, and topological defect dynamics in nanostructures, and so on [8, 9, 10, 12].

Coherent x-ray diffractive imaging relies on the fact that the x-ray beam is non-destructive due to weak interaction with matter. In other words, x-ray radiation does not affect a sample so that its properties and positions are not altered while the sample is rocked to collect 3D diffraction pattern. However, it is sometimes observed that the Bragg peak shifts during rocking scan, which is undesirable. This phenomenon is analyzed based on the conservation of photon energy and wave momentum.

Chapter 2

Coherent x-ray diffraction imaging

This chapter reviews theoretical background needed to understand coherent x-ray diffractive imaging technique commonly used throughout this thesis. X-ray microscopy has been attractive for study of materials structures because of one of characteristics of x-ray beam, diffraction. Recently, the advent of highly coherent and bright x-ray sources at synchrotrons has enabled a lensless imaging technique called coherent diffractive imaging. Since it was first demonstrated in 1999 [13], there has been significant progress in coherent diffractive imaging technique with resolutions approaching a few nanometers. Each fundamental concept for coherent x-ray diffractive imaging such as x-ray diffraction, synchrotron radiation, and phase retrieval will be addressed in this chapter.

2.1 Coherent x-ray diffraction

A measurement of coherent x-ray diffraction pattern followed by phase retrieval has to be performed for coherent x-ray diffraction imaging. In this section, coherent x-ray diffraction, which is fundamental concept for understanding experimental data will be reviewed. The Bragg's Law, which is illustrated in Fig 2.1, and specific description of the x-ray diffraction associated with crystals will be discussed from a crystallographic point of view in the following subsections. In the last, coherent properties which is essential for synchrotron light sources will be discussed.

2.1.1 Bragg's Law

X-rays are a form of electromagnetic radiation and were discovered in 1895 by Wilhelm Conrad Röntgen. Due to the ability of penetration and short wavelength of x-ray, it has been useful and powerful in a wide range of fields such as crystallography, radiography, astronomy and material science.

We exploit the exceptionally coherent high-brightness of x-rays produced by third generation synchrotron sources. The hard x-rays with a wavelength of 1.36 Å ($9keV$) and a bandwidth of $1eV$ were utilized mostly in our experiments. If we assume the incident x-rays are plane waves and it scatters elastically, the diffraction occurs due to interference between spherical waves scattered from the atoms in the crystal. The interference pattern can be explained by the Bragg

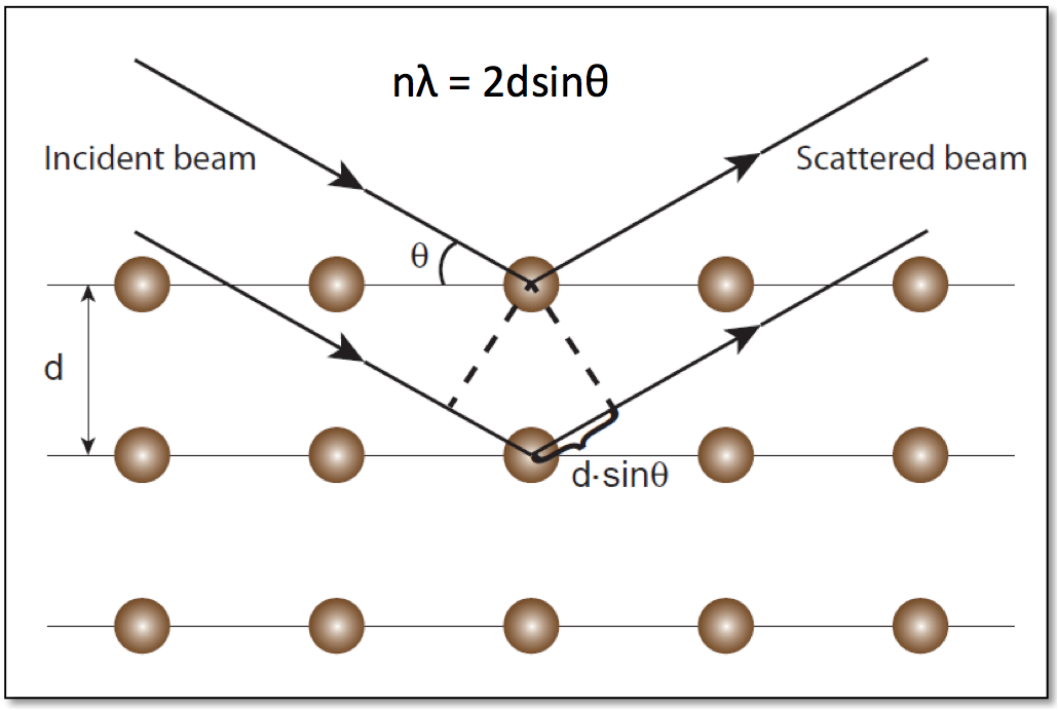

Figure 2.1: Schematic of Bragg's Law. An incident x-ray beam diffracted from atomic layers. If n is an integer, the scattered beam from different layers are perfectly in phase with each other and produce a bright spot in a far field.

Law: The incident waves are scattered from lattice planes separated by distance d. They remain in phase when the path length difference $2dsin\theta$ is an integer multiple of the wavelength. Thus, constructive interference occurs when the phases are equal. Figure 2.1 shows the extra distance traveled by the wave scattered from the second lattice plane is $2dsin\theta$. When that distance is set equal to $n\lambda$ (where n is an integer), the result is Braggs Law $n\lambda = 2dsin\theta$. Bragg diffraction was first proposed by William Lawrence Bragg and his son, William Henry Bragg, in 1913 in response to their discovery that crystalline solids generated special patterns of reflected x-rays.

2.1.2 Diffraction from crystals

An ideal crystalline material consists of regularly repeated basic units, known as unit cells. In a crystalline material, all the atoms are placed highly ordered fashion with periodic positions so that the three dimensional lattice can be defined by a vector set. The scattering amplitude of an atom can be written as [14, 15]

$$A(Q) = -r_0 f(Q) = -r_0 \int \rho(r) e^{iQ\cdot r} dr \tag{2.1}$$

where r_o is the Thomson scattering length, Q is a momentum transfer vector, $f(Q)$ is the atomic form factor, r is the position of atoms, and $\rho(r)$ is electron density. The position of any atom in a crystal can be decomposed into R_n and r_j, where R_n are the lattice vectors and r_j the position of the atoms with respect to particular lattice position. The scattering amplitude for a crystal can be expressed as,

$$A(Q) = -r_0 \sum_n e^{iQ\cdot R_n} \sum_j f_j(Q) e^{iQ\cdot r_j} \tag{2.2}$$

Two terms are called the lattice sum, and the unit cell structure factor, respectively. If the scattered waves interfere constructively, the following equation can be satisfied.

$$Q \cdot R_n = 2\pi \times integer \tag{2.3}$$

The lattice vectors R_n are of the form

$$R_n = n_1 a_1 + n_2 a_2 + n_3 a_3 \tag{2.4}$$

where (a_1, a_2, a_3) are the basis vectors of the lattice and (n_1, n_2, n_3) are integers. A solution to Eq. (2.2) can be found by employing the concept of the reciprocal lattice. The reciprocal lattice is formed by the three basis vectors.

$$a_1^* = 2\pi \frac{a_2 \times a_3}{a_1 \cdot (a_2 \times a_3)}, a_2^* = 2\pi \frac{a_3 \times a_1}{a_1 \cdot (a_2 \times a_3)}, a_3^* = 2\pi \frac{a_1 \times a_2}{a_1 \cdot (a_2 \times a_3)} \tag{2.5}$$

so that any lattice site in the reciprocal lattice is given by

$$G = h a_1^* + k a_2^* + l a_3^* \tag{2.6}$$

where (h, k, l) are all integers. We can obtain the product of a lattice vector in the reciprocal (G) and direct (R_n) spaces is

$$G \cdot R_n = 2\pi \times (h n_1 + k n_2 + l n_3) = 2\pi \times integer \tag{2.7}$$

and therefore, Eq. (2.2) requires that

$$Q = G \tag{2.8}$$

This represents that $A(Q)$ is non-vanishing if and only if Q is a reciprocal lattice vector. This is the Laue condition for the observation of diffraction from a crystalline lattice which is completely equivalent to Bragg's law.

2.1.3 Coherent scattering on finite size crystals

In the preceding section, it was assumed that coherent x-ray radiation illuminates on infinitely extended and ideal crystals. However, in reality crystal is finite and the periodicity is truncated at free surface, which leads to a spreading of intensity distributions around Bragg peaks. The following approach was demonstrated by *Vartanyants et al.* [16].

The finite volume of a crystal is given by the shape function.

$$s(r) = \begin{cases} 1 & \text{x} \in \text{crystal} \\ 0 & \text{otherwise} \end{cases}$$

The infinite lattice of the crystal can be defined by

$$\rho_\infty(r) = \sum_{n=1}^{\infty} \delta(r - R_n) \tag{2.9}$$

where $R_n = n_1 a_1 + n_2 a_2 + n_3 a_3$ is the position of the unit cell (see Eq. (2.4)). The electron density of one unit cell in the crystal can be expressed as

$$\rho_{uc}(r) = \sum_j \rho_j(r - r_j) \tag{2.10}$$

where r_j is a coordinate and $\rho_j(r)$ is the electron density of individual atoms in a unit cell. Now the electron density for a finite size crystal can be written

$$\rho(r) = [s(r) \cdot \rho_\infty(r)] \otimes \rho_{uc}(r) \tag{2.11}$$

where $\otimes$ denotes a convolution.

The electron density can be expressed in terms of a sum of corresponding individual atoms:

$$\rho(r) = \sum_{n=1}^{N} \sum_{j=1}^{S} \rho_{nj}(r - (R_n + r_j) - u(R_{nj})) \tag{2.12}$$

where R_n is the position of the nth unit cell in a perfect lattice, r_j is the coordinate of atom j in this unit cell and $u(R_{nj})$ is the displacement from this ideal lattice point. Replacing Eq. (2.1) with this equation for the electron density, the scattering amplitude can be written as an infinite sum over the unit cells:

$$A(q) = \sum_{n=1} \left(\sum_{j=1} \left(\int \rho_{nj}(r') e^{-iq \cdot r'} dr' \right) e^{-iq \cdot r_j} \right) e^{-iq \cdot u(R_n)} e^{-iq \cdot R_n} \tag{2.13}$$

The term in the inner parenthesis can be replaced by Eq. (2.11) and using the convolution theorem for Fourier transforms, we get the scattered amplitude:

$$A(q) = F(q) \int \rho_{\infty}(r) S(r) e^{-iq \cdot r} dr \tag{2.14}$$

where

$$F(q) = \int \rho_{uc}(r) e^{-iq \cdot r} dr \tag{2.15}$$

is the structure factor of the nth unit cell. It is assumed that the structure factors are identical ($F_n(q) = F(q)$) and integration is carried out over the whole space.

$$\rho_{\infty}(r) = \sum_{n=1}^{\infty} \delta(r - R_n) \tag{2.16}$$

is a periodic function over all points of an infinite ideal lattice. The shape function multiplied by the exponential term regarding displacement is also included

in the integral.

$$S(r) = s(r)e^{-iq\cdot u(r)} \tag{2.17}$$

Equation (2.14) is a Fourier transform of periodic function multiplied by the shape function. Using the convolution theorem, we can get the scattering amplitude as follows.

$$A(q) = F(q) \cdot [\rho_\infty(q) \otimes S(q)] \tag{2.18}$$

This equation can be rewritten based on the definition of convolution.

$$A(q) = \frac{F(q)}{(2\pi)^3} \int \rho_\infty(q')S(q-q')dq' \tag{2.19}$$

where $S(q')$ is the Fourier integral of $S(r)$ and $\rho_\infty(q)$ is the Fourier transform of the lattice function, which reduces to the sum of δ-functions in reciprocal space

$$\rho_\infty(q) = \int \rho_\infty e^{-iq\cdot r}dr = \frac{(2\pi)^3}{v}\sum_n \delta(q-h_n) \tag{2.20}$$

where v is the volume of the unit cell and h_n is the reciprocal space lattice vector. The function $S(r)$ has been introduced in Eq. (2.17). It has the amplitude $s(r)$ and the phase $\phi(r) = q \cdot u(r)$, including the displacement field $u(r)$. The queation (2.19) can be rewritten as follows.

$$A(q) = \frac{F(q)}{v}\sum_n A_n(q-h_n) \tag{2.21}$$

with $A_n(q-h_n) = S(q-h_n)$. The scattered intensity from the finite-sized crystals is determined by a sum over reciprocal lattice points. The small cross-terms are neglected.

$$I(q) = |A(q)|^2 = \frac{|F(q)|^2}{v^2} \sum_n |A_n(q - h_n)|^2 \tag{2.22}$$

When the Laue condition is satisfied for the particular Bragg peak, $h_n = h$ and $q \approx h$, the intensity reduces to

$$I(q) = \frac{|F(q)|^2}{v^2} |A_h(Q)|^2 \tag{2.23}$$

where $Q = q - h$ and

$$A_h(Q) = \int s(r) e^{-ih \cdot u(r)} e^{-iQ \cdot r} dr \tag{2.24}$$

This equation indicates that the scattering amplitude is directly associated with the shape function and the phase factor.

2.1.4 Coherence

A synchrotron facility provides x-ray beams with coherent characteristics and low divergence. Interference is one of the most essential phenomena for x-ray diffractive imaging and it can occur because of coherence effects. The coherence of a beam of light, including undulator x-ray beams has two distinguishable components, both transverse and longitudinal coherence lengths, ξ_T and ξ_L respectively.

The transverse coherence is defined as the lateral distance along a wavefront over which the phase is completely canceled out, which result from two separate points in space. If we assume that the two waves emit from points with a small angular separation $\Delta\theta$, the transverse coherence length is given by:

$$\frac{\lambda}{2\xi_T} = tan\Delta\theta \approx \Delta\theta \tag{2.25}$$

$$\frac{D}{R} = tan\Delta\theta \approx \Delta\theta \tag{2.26}$$

$$\xi_T = \frac{\lambda R}{2D} \tag{2.27}$$

where λ is the wavelength of incident x-ray and $\Delta\lambda$ is the difference in wavelength between different incident waves, and D is the finite source sizes of accelerated electrons from which x-ray is produced, R being the distance the incident x-ray travels and it is considered that $R \gg D$, and it is the distance between sample and x-ray detector.

The longitudinal coherence is defined as the distance over which two waves from the same source point with slightly different wavelengths will be completely out of phase. Two waves of slightly different wavelengths λ and $\lambda - \Delta\lambda$ are emitted

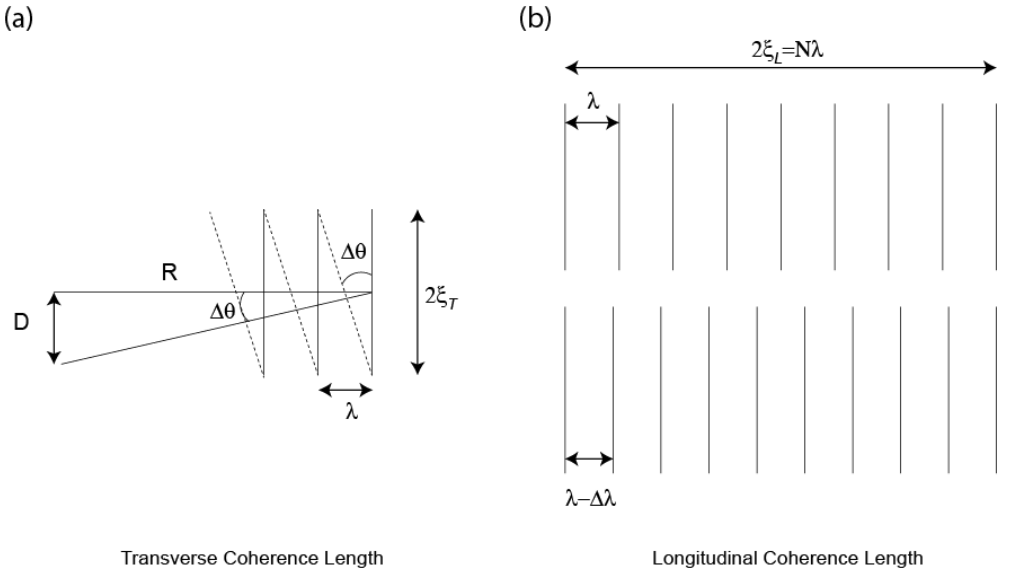

Figure 2.2: Transverse coherence length and longitudinal coherence length, repectively. (a) Two waves emitted from different sources interfere until the waves are out of phase is called transverse coherence length $2\xi_T$. (b) Two waves with slightly different wavelength are emitted in the same direction. The distance between two phase matches is defined as $2\xi_L$.

from the same point in space simultaneously. The two waves will be exactly out of phase after a distance ξ_L, followed by in phase after ξ_L more.

$$\xi_L = \frac{\lambda^2}{2\Delta\lambda} \tag{2.28}$$

The longitudinal coherence is dependent on the bandwidth of the monochromator ($\Delta\lambda/\lambda$). This is related to the Optical Path Length Difference (OPLD) of x-ray through the sample. In order to meet the requirement for coherent x-ray diffraction measurement, the OPLD has to be smaller than the sample size. The longitudinal coherence length at 34-ID-C at the Advanced Photon Source was determined to be, ξ_L= 0.66μm [17].

Equation (2.21) can be rewritten taking time into account [16].

$$A(q',t) = \frac{F(q)}{v} \sum_n A_n(q' - h_n, t) \tag{2.29}$$

where

$$A_n(q,t) = \int dr\ s(r) A_{in}(r, t - \tau_r) e^{-iq\cdot r} \tag{2.30}$$

Here, τ_r is the time delay for the radiation propagation between the same points. The intensity near the one of Bragg points, $h_n = h$:

$$I(Q) = \left\langle A(Q,t)A^*(Q,t)\right\rangle_T = \frac{F(h)^2}{v^2}|A_h(Q,t)|^2 \tag{2.31}$$

$$= \frac{F(h)^2}{v^2} \int\int dr dr' s(r)s(r')\Gamma(r,r',\Delta\tau)e^{-iQ\cdot(r-r')} \tag{2.32}$$

where $\Delta\tau$ is a time delay and $\Gamma(r,r',\tau) = \left\langle A(r,t)A^*(r',t+\tau)\right\rangle_T$ is the mutual coherence function. It can be expressed as a product [18].

$$\Gamma(r,r',\tau) = \sqrt{I(r)}\sqrt{I(r')}\gamma(r,r')F(\tau) \tag{2.33}$$

where $I(r) = \left\langle |A(r,t)|^2\right\rangle_T$ and $I(r') = \left\langle |A(r',t)|^2\right\rangle_T$ are the averaged intensities of the incoming radiation at points r and r', $\gamma(r,r')$ is a normalized mutual coherence function and $F(\tau)$ is the time autocorrelation function.

If the x-ray beam is completely coherent, $\Gamma(r,r',\tau) = \sqrt{I(r)}\sqrt{I(r')}$ and if it is partially coherent, $\Gamma(r,r',\tau) < \sqrt{I(r)}\sqrt{I(r')}$. Thus, the value of $\gamma(r,r')F(\tau)$ represents the degree of coherence.

2.2 Synchrotron Radiation

Synchrotron radiation has a large impact on nanoscience and interdisciplinary science. Many scientific research area have been tremendously successful with the advent of synchrotron x-ray sources. A synchrotron radiation source is a storage ring in which the charged particles are accelerated radially. It produces highly coherent and brilliant x-ray beam using bending magnets that keep the electron beam on its circular path.

The first generation synchrotron light sources were parasitically on accelerations for particle physics studies in 1950s [19] . The second generation synchrotron light sources were designed for the production of synchrotron radiation and employed electron storage rings. The third generation sources started operation in the early 1990s. The synchrotron light sources optimize the intensity of the light by incorporating insertion devices into the storage ring. The insertion devices consist of a periodic sequence of dipole magnets with alternating orientation, and force the electron beam on a trajectory. Wigglers create a broad but intense beam of incoherent light. Undulators create a narrower and significantly more intense beam of coherent light, with selected wavelengths, or harmonics, which can be tuned by manipulating the magnetic field in the device [20]. Laboratories around the world are now working to overcome the technical challenges associated with the development of fourth-generation light sources, which are likely to utilise hard x-ray free-electron lasers (FEL).

2.2.1 X-ray beam source

Synchrotron radiation is simply radiation from electrons moving in a uniform magnetic field. The acceleration of an electric charge leads to the emission of electromagnetic waves. However, synchrotron sources can achieve x-ray beams that have high frequencies due to the relativistic effects [21]. The emitting electrons travel at nearly speed of light c. This leads to a series of relativistic effects that bring the emitted frequencies to the x-ray regime. In addition, the extreme angular collimation of the emitted x-rays is possible due to relativistic effects.

The relativistic frame change rules show that the electron sees an oscillating magnetic field and an oscillating electric field in the perpendicular direction in the undulator. Its wavelength in the electron frame, L/γ, equals the undulator period L after Lorentz contraction by the 'γ-factor'. Here, the γ characterizes the relativistic properties of the moving electron, and is defined as the electron energy mc^2 divided by its Einstein's rest energy, $m_o c^2$:

$$\gamma = \frac{mc^2}{m_o c^2} \tag{2.34}$$

We use the standard relativistic factors $\beta = u/c$ and $\gamma = 1/\sqrt{1-\beta^2}$. The corresponding wavelength in the laboratory frame is subject to the Doppler effect. The multiple Doppler factor is $\sqrt{(1-\beta)}/\sqrt{(1+\beta)} \approx 1/2\gamma$ because the relativistic factor β is close to 1.

The emitted wavelength in the laboratory frame is:

$$\lambda \approx \frac{L}{2\gamma^2} \tag{2.35}$$

Therefore, the macroscopic undulator period can be transformed into the angstrom-size wavelength of x-ray due to the relativistic effects such as Lorentz contraction and Doppler shift. These relativistic effects shrink the wavelength by a factor $2\gamma^2$.

In practical, the energy of an electron beam that are generated at Advanced Photon Source is 7GeV with $\gamma \approx 10^4$. Table 2.1 presents a brief list of the main parameters of these sources in operation world-wide [19]. The electron energy is an important parameter since it determines the size of the facility and a wavelength of beam in the x-ray regime.

Table 2.1: The list of synchrotron light sources.

The parameters of high and intermediate energy synchrotron light sources [19].

Name	Location	Energy (GeV)	Perimeter (m)	Emittance (nm rad)
SPRING-8	Japan	8	1436	3
APS	US	7	1060	3
ESRF	France	6	844	3.8
PLS	Korea	2.5	281	12
ANKA	Germany	2.5	240	70
SLS	Switzerland	2.4	240	5
ELETTRA	Italy	2-2.4	260	7
Nano-Hana	Japan	2	102	70
ALS	US	1.9	197	6.8
BESSY-II	Germany	1.7-1.9	240	5.2

2.2.2 The brilliance

The quality of a synchrotron source can be assessed with several parameters. The brilliance is one of major parameters to reflect the capability of x-ray sources. It is a combination of the radiation flux, the angular divergence of the light, and the size of source [20, 22]. A excellent brilliance implies a high x-ray radiation flux, a small angular divergence, and a small size of a source. Therefore, a source can be made brighter by increasing the flux, by decreasing the size or by enhancing the angular collimation.

$$Brilliance = \frac{The\ number\ of\ photons/s}{(mrad)^2\ (mm^2\ source\ area)(0.1\%\ bandwidth)} \tag{2.36}$$

The beam intensity (in units of photons per second) after the monochromator can be further calculated as the a product of the brilliance, angular divergences set by the horizontal and vertical apertures (in milli-radian), the source area (in mm^2) and the bandwidth of the monochromator relative to 0.1%. Where the source flux is given as the number of photons per second per unit surface area.

Modern hard X-ray third generation synchrotron sources such as the Advanced Photon Source (APS) in the United States, the European Synchrotron Radiation Facility (ESRF) in France, and the Super Photon Ring-8 (SPring-8) in Japan operate with a brilliance (or equivalently brightness) at or above $10^{19}(photons/s/0.1bw/mm^2/mr^2)$.

2.2.3 Beamline setup

The beamline 34-ID-C at APS is optimized for Bragg coherent x-ray diffractive imaging. It consists of an undulator, primary slits, a Si(111) monochromator, aperture, Kirkpatrick-Baez (KB) focussing mirrors, a goniometer, devices for precise translations of a stage, and a detector [23].

The primary slits define a beam of 150 microns in the horizontal and are open (guarding) in the vertical. The coherence-defining slits (50m) are usually set to 50×20 microns (V×H) since the vertical coherence length (90μm) is determined by the source size, the horizontal (25μm) by the primary slit and the longitudinal (0.5μm) by the monochromator [24]. The monochromator is used to select 9.0 keV monochromatic x-rays ($\lambda = 1.39\mathring{A}$) with a bandwidth (1eV) small enough to provide a longitudinal coherence length. Focused beams act as local probes allowing to investigate submicron parts of an extended sample. Kirckpatrick-Baez (KB) mirrors are reflective optics at near-glancing angle of incidence, largely used today with hard x-rays. They consist of two mirrors that are bent with elliptical profile and are aligned orthogonally with respect to each other to focus to the same point. A deviation from orthogonal alignment can cause both mirrors to be defocused. The enlargement of the focal spot can be achieved by the mirror rotations in three directions. The aperture is placed before the mirrors and adjusted so that x-ray beam illuminates a given area of the KB mirror surfaces.

The nanocrystals on the stage are centered and aligned in the focussed beam. The stage moves the sample into the beam, illuminating all crystals in the beam foot-print. The beam footprint on the sample is dependent on incident angle. As the incident angle decreases, the illuminated area on the sample, which is beam footprint will increase accordingly. The footprint is varied to locate and isolate crystals on the substrate.

A laser scanning confocal microscope is attached to the diffractometer above the sample. Three objective lenses (5x, 10x, and 20x)are fitted to the microscope [25]. A Charge-Coupled Device (CCD) area detector with 22.5 μm pixel size is placed away from the sample so that the fringes arise sufficiently. The position of the detector is governed by a particular Bragg angle. The coverage of the Bragg angle is subject to the constraints of the movement of CCD detector arm. The nanocrystal is rocked through the Bragg peak with small steps to sample the intensities sufficiently. A complete 3D diffraction pattern of the Bragg peak can be obtained by collecting the 2D diffraction patterns that are oversampled in all directions with respect to the spatial Nyquist frequency, which is inverse of the sample size. In practice, to ensure correct oversampling, the amplitude has to be sampled at least at both peaks and troughs, which meets sampling requirement for phase retrieval.

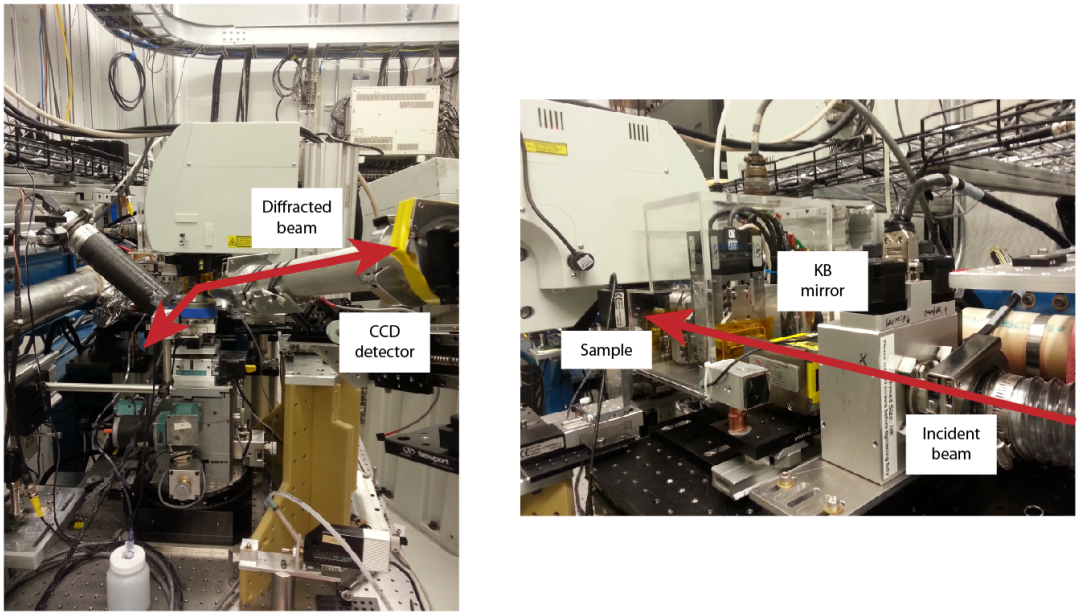

Figure 2.3: Image of experimental setup at 34-ID-C beamline in Advanced Photon Source. An incident x-ray beam comes from the undulator is focused by KB mirror and illuminated an sample (right image). A diffracted x-ray beam goes into CCD detector (left image).

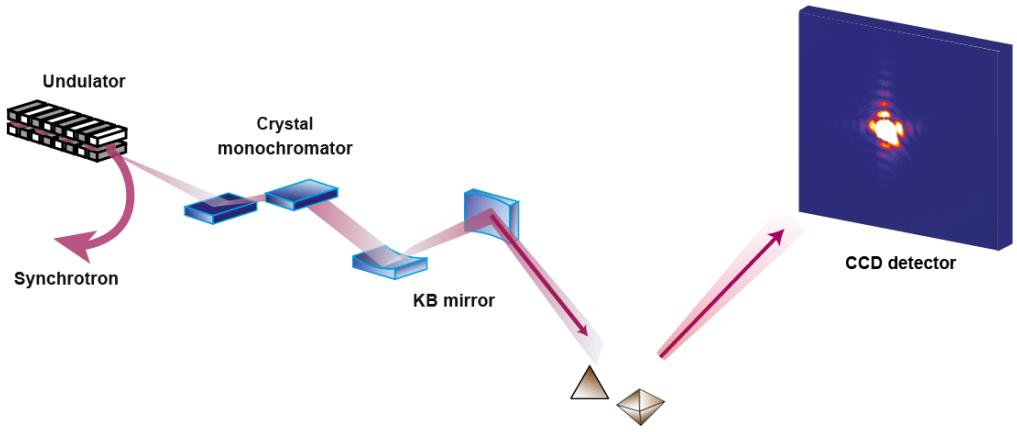

Figure 2.4: Schematic of the experimental set-up and sample at 34-ID-C beamline in Advanced Photon Source. Monochromatic x-ray beam of wave vector impinges on to Kirkpatrick-Baez mirrors, which creates a localized illumination on the sample. Coherent x-ray diffraction patterns are recorded with a two-dimensional pixelated detector.

2.3 Phase Retrieval

The fact that the intensities ($I = |E|^2$ where E is the amplitude of the diffracted wave) are measured with the loss of information regarding the phase of the waves gives rise to the so-called phase problem. It has been a recurring issue in crystallographic reconstructions although a significant research effort has been made to develop a method to solve the phase problem over most of the past hundred years. None of methods provide the solution to the phase problem directly. It can be mitigated on the condition that the sampling frequency in reciprocal space is at least twice the bandwidth of the real space frequency, which is called oversampling [26, 27]. If we use iterative algorithm that goes back and forth between real and reciprocal space, we can get a converged solution. The algorithm starts with 'first guess' and applies constraints in each space during iteration. By employing an iterative algorithm, the phase information from the oversampled diffraction data of a nanocrystal has been successfully retrieved.

2.3.1 Oversampling

According to the Shannon sampling theorem which is introduced in 1949, to record all the signal information, the sampling frequency must be at least twice of the maximum present frequency [28]. In 1952, Sayre reasoned that the lost phase information of a scattered x-ray beam might be recovered if the Bragg diffraction intensity are measured at Nyquist frequency (the inverse of the size of the diffract-

ing specimen) [29]. This is a result of the fact that if the original signal $A(q)$ can be written as the Fourier transform of $\rho(r)$,

$$A(q) = \mathcal{F}\{\rho(r)\} \tag{2.37}$$

then its square modulus $I(q) = A^*(q)A(q)$, where $A^*(q)$ is the complex conjugate of $A(q)$ then $I(q)$ can be written as the Fourier transform of the autocorrelation function.

$$I(q) = \mathcal{F}\{\rho(r) \otimes \rho(r)\} \tag{2.38}$$

Because the maximum possible extent of the autocorrelation of a discrete function is twice the size of the extent of the original function, the band limit of $I(q)$ is twice that of $A(q)$. Therefore, it has to be ensured that a sampling frequency is finer than Nyquist frequency. In a practical way, the no-density region should be larger than the electron-density region so that sufficient data points are collected to retrieve phase information [26, 27].

$$\sigma = \frac{no\ density\ region + electron\ density\ region}{electron\ density\ region} \tag{2.39}$$

The phase retrieval from an oversampled diffraction pattern is possible if the ratio σ is larger than 2 [30].

2.3.2 Gerchberg-Saxton Algorithm

In 1972, Gerchberg and Saxton proposed a method to recover the phase of wavefront knowing both a density of sample and its diffraction pattern [31]. In other words, the constraints to the algorithm are the amplitudes of the images in both spaces and they should be known.

The phases are initially generated randomly between π and $-\pi$. These are then multiplied by the respective sampled image amplitudes and are taken Fourier Transform. The phases of the complex function resulting from this transformation are calculated and combined with the corresponding sampled diffraction intensity. This function is then inverse Fourier Transformed, the phases are computed and combined with the sampled image amplitude function to form a new estimate of the complex sampled image and the process is repeated [31].

The procedure can be summarized as follows:

1. Fourier transform the current estimate of image.

2. Replace the magnitude of the resulting image with the known amplitude to form a new estimate of the image in reciprocal space.

3. Inverse Fourier transform the estimate of image.

4. Replace the magnitude of the resulting image with the known amplitude to form a new estimate of the image in real space.

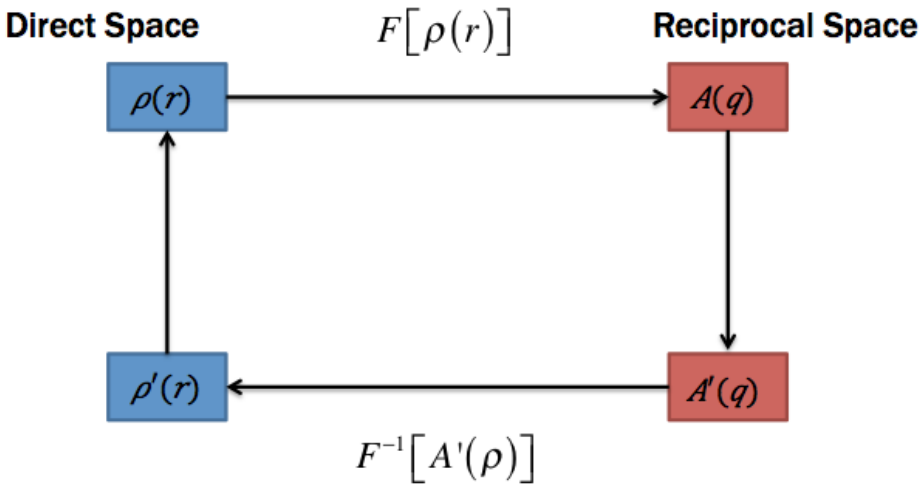

Figure 2.5: A diagram of Gerchberg-Saxton algorithm. A loop between real and reciprocal space by means of Fourier Transformation back and forth and using constraints in each space.

2.3.3 Fienup Algorithm

As mentioned in previous section, Gerchberg and Saxton developed an iterative algorithm that would reconstruct amplitudes and phases of an object from intensity measurement $|f|$ in real space and a measurement of the Fourier modulus $|F|$ in reciprocal space. The algorithm iterates and exploits the modulus constraint in both spaces, while keeping phases updated. Fienup improved on the Gerchberg-Saxton algorithm to reconstruct phase information just using measurement of the Fourier modulus in reciprocal space, without measuring $|f|$ which is essential for the Gerchberg-Saxton algorithm [32]. In the algorithm which is called error-reduction (ER) algorithm, the modulus constraint is applied in the reciprocal space. The Gerchberg-Saxton algorithm and ER algorithm were widely used to solve phase problem.

$$\rho_{k+1}(x) = \begin{cases} \rho_k^{'}(x) & \text{x} \in \text{S} \\ 0 & \text{otherwise} \end{cases}$$

where S represents a finite support whose size has to be at most 1/8 of entire density in three dimensional space. All data outside the support, where an object is assumed to exist, are set to zero. In reciprocal space, the modulus which is Fourier transformed from real space has to be replaced with the square-root of measured intensity. These steps are repeated until the convergence of the algorithm.

Although the ER algorithm minimizes the error throughout the iterations, it suffers from the failure of convergence and stagnation problems. Fienup proposed a hybrid input-output algorithm (HIO) to avoid local minima and approach the vicinity of the global minimum [32, 33, 34]. This algorithm differs from the error-reduction algorithm in the object domain.

$$\rho_{k+1}(x) = \begin{cases} \rho_k^{'}(x) & \text{x} \in \text{S} \\ \rho_k(x) - \beta\rho_k^{'}(x) & \text{x} \notin \text{S} \end{cases}$$

where S represents a finite support and β is a parameter ranges between 0.5 and 1. In reciprocal space, constraint is applied in the same manner as in ER algorithm. But in the real space, the current input $\rho_{k+1}(x)$ is made up of a combination of the previous input $\rho_k^{'}(x)$ and the output $\rho_k(x)$. This algorithm is much stronger in avoiding stagnation and local minima. The combination of HIO and ER algorithm consists of iterations of the HIO algorithm followed by iterations of the ER algorithm. This combination is more successful than both algorithms on their own as it was observed in practice [33, 34]. To date variations on the existing ER and HIO algorithms have been used as iterative approaches to the phase problem in the form of Millanes HIO [35] and Solvent Flipping (SF) [36]. Alternative algorithms include Difference Map (DM) [37], Averaged Successive Reflections (ASR) [38], Hybrid Projection Reflection (HPR) [39] and Relaxed Averaged Alternating Reflectors (RAAR) algorithm [40].

2.3.4 Shrink-wrap

In 2003 Marchesini et al. proposed a method for the reconstruction algorithms, the so-called shrink-wrap algorithm [41]. The main idea is that this method allows a support to change in certain intervals during the iterative reconstruction process. A support in a real space is one of main constraints in the reconstruction algorithm. If the shrink-wrap is used, the support is refined during reconstruction based on a thresholding operation so that it helps the convergence of the algorithm.

2.3.5 Uniqueness

The phase-retrieval real space density distribution is well-known to have a two-fold degeneracy because the combination of inversion symmetry and complex conjugate to any complex function solution can be an indistinguishable solution, resulting in identical experimental data [33]. This non-uniqueness problem arises because diffraction is inherently centrosymmetric with all intensity. Consider an image denoted by $f(x)$, where x is the position vector in real space. The Fourier transform of the image, or the visibility, $F(u)$ is given by

$$F(u) = \int_{-\infty}^{\infty} \rho(x) exp(i2\pi u \cdot x) dx \tag{2.40}$$

where u is the position vector in reciprocal space. The image is given by the inverse Fourier transform of the visibility, so that

$$\rho(x) = \int_{-\infty}^{\infty} F(u) exp(i2\pi x \cdot u) du \tag{2.41}$$

and recovery of the image is straightforward if $F(u)$ is measured. A phase problem arises when only the amplitude $|F(u)|$ can be measured. Since the image is given uniquely by Eq. (2.40), recovery of the image is equivalent to recovering the phase $\phi(u)$, where

$$F(u) = |F(u)| exp[i\phi(u)] \tag{2.42}$$

As a result of the autocorrelation theorem, the autocorrelation $A(x)$ of the image, where

$$A(x) = \int_{-\infty}^{\infty} \rho(y)\rho^*(x+y) dy \tag{2.43}$$

can be reconstructed from the magnitude, since $|F(u)|^2$ is the Fourier transform of $A(x)$. Therefore, the complex density image, $\rho(x)$, obtained from Fourier inversion of the measurement is indistinguishable from $\rho^*(x)$.

One of these two solutions is arbitrarily picked in the phasing algorithm. There is no direct method to determine the 'correct' solution for phase information. In order to identify the uniqueness of the solutions of the phase retrieval algorithms, practically prior knowledge such as SEM image or optical microscopy images, are used. But if an absolute phase value is needed for very symmetric object, additional information is needed [12].

Chapter 3

Theoretical background for equilibrium crystal shape

3.1 Wulff construction

Wulff Victorovich (George) Wulff was a Russian crystallographer known in crystal growth theory for his construction of the ideal equilibrium form (Wulff, 1902). So-called Wulff plots are constructions used to predict the equilibrium form of crystals. He developed the construction of the stereographic net as an equivalent to the stereographic projection (Wulff, 1908) [42]. This theory was not proved until Conyers Herring demonstrated the method to determine the equilibrium shape of a crystal based on a polar plot of surface energy as a function of orientation in 1953 [43].

For an equilibrium crystal, the distance between a center of a crystal and any given surface facet is proportional to the surface free energy of that facet. This statement can be expressed as follows [44]:

$$\frac{\gamma_1}{l_1} = \frac{\gamma_2}{l_2} = ... = \frac{\gamma_i}{l_i} \tag{3.1}$$

where γ_i is the specific surface free energy of the i^{th} crystal plane and l_i is the central distance of the i^{th} crystal plane. It is applicable to the equilibrium crystal shape (ECS) in not only two dimensions, but also can be extended to three dimensions in spherical coordinates is typically utilized to describe ECS.

If a γ plot that represent the anisotropy of the surface tension by drawing a vector from the origin is given, the equilibrium crystal shape can be identified based on the concept that the crystal minimize total surface energy in a given volume. It is obvious that the planes on the cusps of the γ plot have low energies. Thus, if there are cusps in the γ plot, the equilibrium shape would be determined in such a way that it contain facets made up by those planes [45].

The procedure to construct the equilibrium crystal shape at fixed temperature is shown in Fig 3.1. In order to obtain equilibrium crystal shape, we need to make a polar plot of the specific surface free energy γ as a function of local orientation and draw all tangents around γ plot. The inner contour inside the polar plot will represent the equilibrium crystal shape.

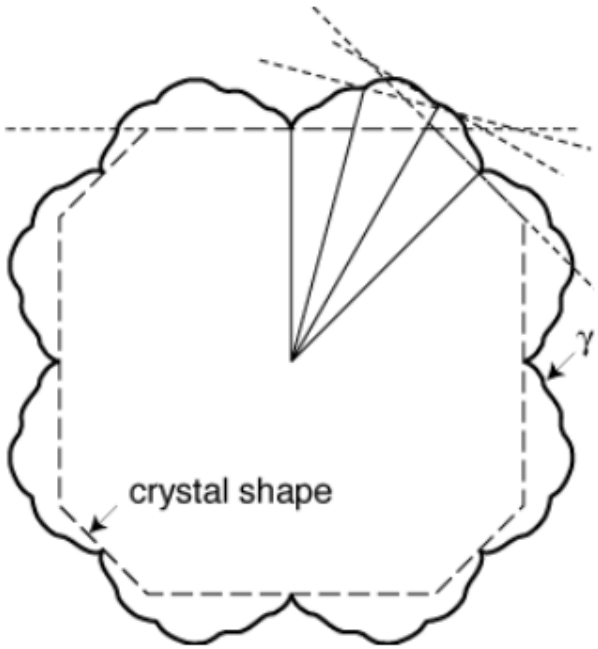

Figure 3.1: The Wulff construction. The Wulff plot constructed by placing points in various directions corresponding to the surface energy for a plane with that direction as the normal [45].

3.2 Young-Laplace (Gibbs-Thomson) equation

A pressure on a side of the surface which is different from the pressure in the other side can cause a normal force, which is proportional to the pressure difference and surface area, to arise and lead to curved surface. This is the Young-Laplace equation developed by Thomas Young in 1804 [46] and independently studied by Pierre Laplace in 1805. This equation originates from fluid statistics with capillary pressure difference across the interface, interfacial tension, and curvature, which is equivalent to the inverse of the radius, of the interface.

This equation can be applicable to various systems such as the raindrops, soap bubbles, and nanopoweders that are associated with surface tension.

$$\Delta P = \frac{2\sigma_s}{R} \tag{3.2}$$

In nanocrystals, the equations for the lattice distortion and surfaces stress have been established based on the Laplace-Young equation. Recently, it has been used to observe the change in lattice parameter of nanopowders [47]. If there are surface stresses on a rounded surface of particle, the pressure difference between the inside and outside can be evaluated using this equation. It is proportional to the surface stress, which is usually tensile in the range of 2 N/m for metals [48, 49], and the curvature of the rounded surface.

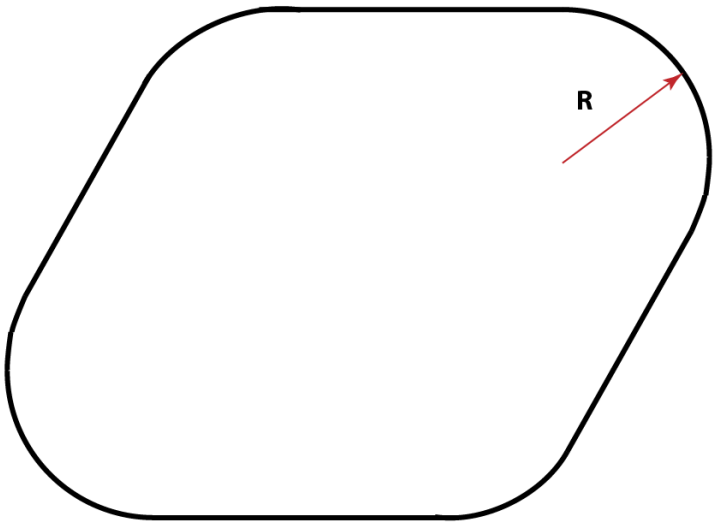

Figure 3.2: A locally rounded surface with radius R. A locally rounded surface with radius R is determined Young-Laplace (Gibbs-Thomson) equation.

Equation (3.2) can be rewritten using materials property and the change of lattice constant so that the strain in the rounded surface can be estimated quantitatively.

$$\frac{\Delta a}{a} = \frac{2\sigma_s}{3KR} \tag{3.3}$$

where bulk modulus, K, of the material, radius R, lattice constant a. This equation will be used for polyhedral gold nanocrystal to compare the theoretical prediction with the one results from the reconstruction of diffraction pattern in Chap. 5.

Chapter 4

Coherent x-ray diffractive imaging of Ni nanocube

Ni-YSZ (Nickel-Yttria-stabilized-Zirconia) materials are being developed for implementation as anodes in solid oxide fuel cells (SOFC). Due to difficulties in storing and transporting pure hydrogen gas, there has been significant effort invested in SOFC anode materials capable of functioning with complex hydrocarbons like natural gas [50]. In this case, sulfur impurities in the fuel stream can poison the anode leading to degraded function. This poisoning likely occurs with the formation of Nickel Sulfides at the triple phase boundaries (TPB) within the anode. The TPB is widely accepted as the catalytically active site in the anode, where the fuel gas is oxidized, and is the boundary between Nickel, YSZ and electrolyte. The formation of Nickel Sulfides at these points in the material effectively blocks the power generating reaction.

4.1 Chemical vapor deposition

Chemical vapor deposition (CVD) can be classified by the method employed to apply the energy necessary to activate the reaction (i.e. temperature, photon, or plasma). We used temperature-activation process commonly known as thermal CVD. In typical thermally activated CVD, high substrate surface temperature is required to provide sufficient energy for diffusion and chemical reactions to take place during the CVD process. In a thermal chemical vapor deposition process, the resulting products are strongly dependent on the growth parameters such as temperature, pressure, moisture on samples, and so on.

During a chemical vapor deposition process, the complicated reactions occur based on the thermodynamics, mass transport, and chemistry. The net change in energy for the reaction needs to be negative in terms of thermodynamics. As the gaseous mixture flows across a solid surface there is a boundary layer directly over the surface through which the reactants will diffuse. Following diffusion through the boundary layer, adsorption onto the surface takes place and reactions occur on this solid surface. Next, any reaction by-products and other escaping atoms/molecules will desorb from the surface and diffuse back through the boundary layer where it will then be carried off with the main stream of flow outside the boundary layer.

Figure 4.1: Lindberg Blue furnace for thermal chemical vapor deposition.

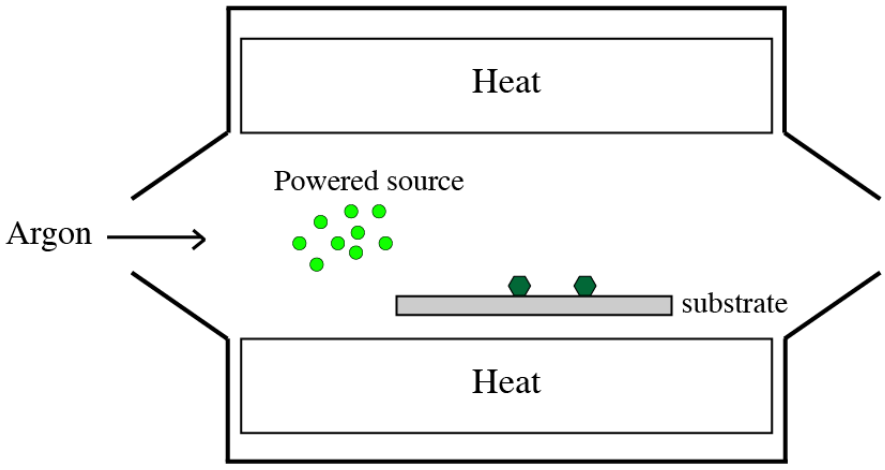

Figure 4.2: Schematic of a CVD reactor.

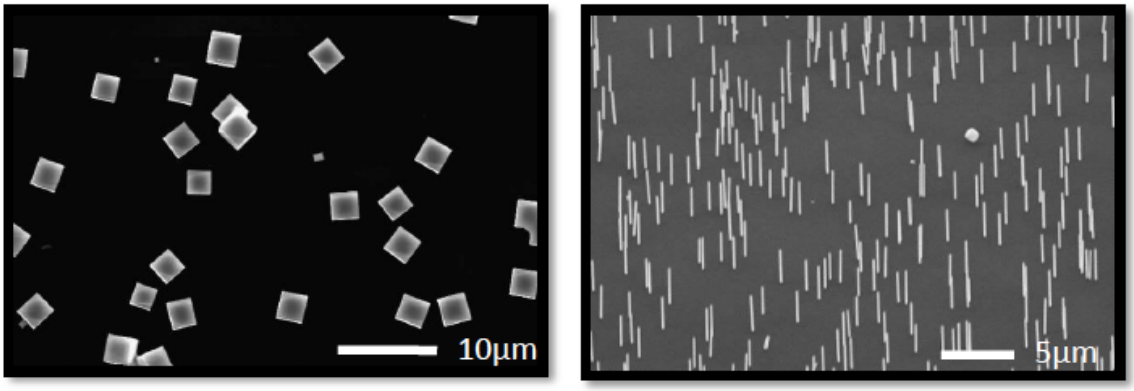

Figure 4.3: Nickel nanocubes grown at low temperature, 600^{o}C and nanowires grown at higher temperature, 650^{o}C [51].

4.2 Growth of Ni nanocrystals

Chemical vapor deposition (CVD) is a promising technique for the synthesis of a wide range of nanostructured materials. Recently, *Chan et al.* [52, 51] extended a traditional CVD process to achieve a significantly increased degree of morphological control for the growth of Ni nanostructures onto $SiO_2||Si$ substrates. This approach has been proved to be high-performance and low-cost method to grow Ni nanowires. The isolation of several distinct nanostructured Ni products in a well-controlled chemical vapor deposition process has been demonstrated [51].

Nickel chloride hexahydrate is used as the precursor material for Ni deposition onto 500nm amorphous $SiO_2||Si$ substrates. The growth parameters such as the moisture content and temperature is varied to achieve the various nanostructured products. Ni nanocubes and vertically oriented Ni nanowires are distinctively synthesized by ramping temperature from 200°C to 650°C and 600°C, respectively, at a rate of 25°C/min following thorough thermal dehydration of the precursor at 200°C (Figure 4.3) [51]. High temperature growth with moisture results in polycrystalline, core-shell structured NWs. Several distinct shapes are created due to the use of an amorphous SiO_2 growth surface that allows liberation from the constraints inherent in epitaxial substrate - deposit relationships resulting in greater flexibility [51]. This study of Ni nanostructure growth can be slightly modified for the growth of other materials. This approach was employed to form single-crystal polyhedral gold nanocrystals.

4.3 Results and discussion

We have measured a diffraction pattern of Ni nanocube, which has a 4-fold symmetry and got preliminary result of reconstruction as shown in Fig 4.4. Figure 4.4 (a) shows local value of phase on the surface of Ni nanocube. The momentum transfer vector is normal to the substrate so that the phase is interpreted as the displacement along vertical direction. The fact that the phase distribution looks mostly red near the bottom surface indicates that the atoms move up. This is consistent with the recent study about the displacement in the metallic nanocrystals [53]. The displacement at the bottom surface is substantially larger than the one at top surface. It is attributed to the interfacial strain from the substrate surface. The strain distribution which is obtained by taking derivative of the displacement as shown in Fig 4.4 (b) shows that there is compressive strain predominantly along vertical direction and the atoms at the top surface are move towards the center of the nanocube.

This results from the reconstruction of the diffraction pattern which is measured without sulfur poisoning. The measurement with the same Ni nanocube should be done under the circumstances with sulfur poisoning. Our goal is to understand which crystallographic surface facets on the nanocrystal impact the poisoning process in SOFCs. There may be obvious changes in the production of Ni-YSZ anodes as a result of a deeper understanding of which facets are more easily poisoned.

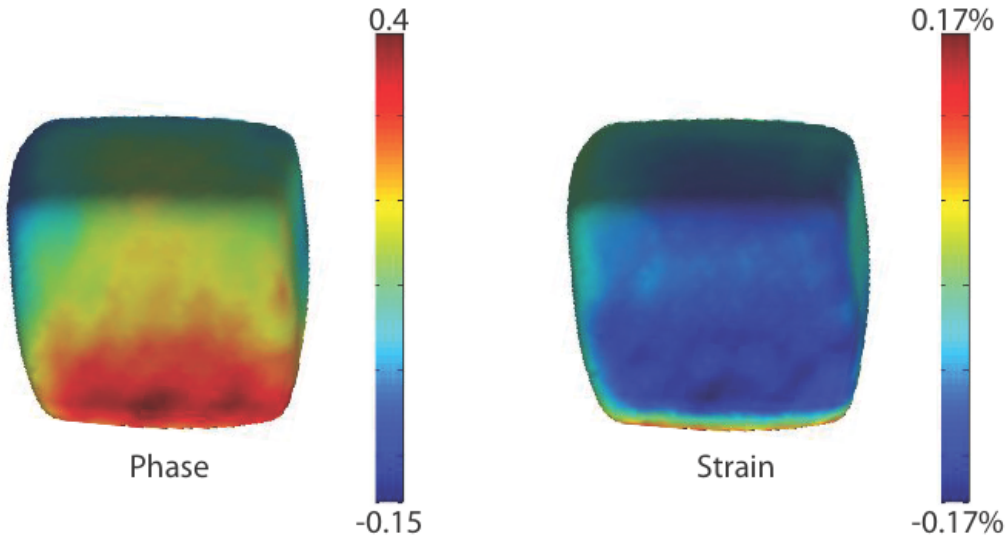

Figure 4.4: Results of reconstructed phase and strain for the nickel nanocube.

Chapter 5

Coherent x-ray diffractive imaging of polyhedral gold nanocrystals

Au nanocrystals were grown using thermal chemical vapor deposition (CVD) onto a Si (100) substrate. A wide range of polyhedral Au nanocrystals with well-defined facets were produced. These nanocrystals are relatively pure because this approach requires neither surfactants nor catalysts of any kind. We were able to study the intrinsic and extrinsic effects on the strain of metallic nanocrystals so that we use coherent x-ray diffractive imaging to map the local distribution of strain in gold polyhedral nanocrystals grown on a silicon substrate by a single-step thermal chemical vapor deposition process. The lattice strain at the surface of the octahedral nanocrystal agrees well with the predictions of the Young-Laplace equation quantitatively, but exhibits a discrepancy near the nanocrystal-substrate interface.

5.1 Introduction

Gold nanocrystals are attracting increasing interest within the scientific community due to the inherent differences between their optical and electronic properties and those of their bulk counterparts [54]. Gold nanocrystals are important for a wide range of potential applications in photonics, nanoelectronics, biological imaging, and biosensors [1, 2, 3, 4] due to their ability to enhance signal in surface plasmon resonance (SPR) absorption and surface enhanced Raman spectroscopy (SERS) measurements, as well as their chemical and thermal stability. The optical and electronic properties of these nanocrystals are strongly dependent on the morphology, size, and strain [55, 56]. Thus, the investigation of nanoscale internal structure, shape, and lattice strain is crucial for the development of suitable synthesis techniques and in understanding growth dynamics on the nanoscale. It has been unclear whether the strain distribution in metallic nanocrystals is intrinsic or if it is a consequence of surface contamination and interfacial stress from the substrate [57]. Au nanocrystals with a face centered cubic (fcc) lattice are characterized by different surface energies for different crystallographic planes. The low-index facets (e.g. (111)) have the smallest specific surface energies that can be found in fcc crystals [58]. The Wulff construction theorem [44], which has been used to predict the equilibrium shape of nanoparticles, offers a geometrical approach to determining the facets which minimize the surface energy of a free floating nanoparticle.

We map the internal strain of Au nanocrystals and find the strain is influenced both by their interaction with the substrate as well as the details of the facet geometry. Coherent x-ray diffractive imaging (CXDI) is a technique that probes the overall shape of a nanostructure [5] and the displacement of individual atoms from an ideal periodic lattice [6, 7, 8, 9, 10]. A mathematical inversion of the coherent x-ray diffraction pattern results in a complex-valued density function. The amplitude of this complex function is proportional to the electron density in the crystal, while the phase can be interpreted as the deformation of the lattice as projected onto the momentum transfer vector, which is determined by the direction of incident and scattered x-ray, of the Bragg peak [59]. The fact that the intensities ($I = |E|^2$, where $I = E$ is the amplitude of the diffracted wave) are measured with the loss of information regarding the phase of the waves gives rise to the so-called phase problem [60]. The phase problem has been a recurring issue in crystallographic reconstructions for many decades. However, it can be mitigated on the condition that the sampling frequency in reciprocal space is at least twice the bandwidth of the real space frequency [26, 27].

5.2 Growth of Au nanocrystals

There have been so many different ways of synthesis for gold nanocrystals. In most cases, the surfactants play important role in controlling crystal growth. The concentration of surfactants and/or the ratio between the surfactant and the co-surfactant are critical to producing well-defined sizes and shapes of gold nanocrystals. However, we obtained various shapes of gold nanocrystals without surfactants or catalysts of any kind, which is one of advantages for this approach.

The approach we used is similar to one that has been used to form Ni nanocrystals [52] and yields single-crystal gold nanocrystals with well-defined facets. The operating temperature is 475°C, which is about 150°C lower than that for Ni nanostructures and the gold nanocrystals were grown on a Si (100) substrate, not on SiO_2||Si substrate. Au nanocrystals were grown with the native oxide using a catalyst-free thermal approach with $AuCl_3$ as a precursor. Approximately 1.0 g of powdered $AuCl_3$ was loaded in a boat and placed within a quartz tube at the center of a Lindberg Blue furnace at 475°C, where the silicon substrate still remains unoxidized because the oxidation of silicon is performed above 800°C [61]. An Ar carrier gas was flowed through the quartz tubing while the downstream end of the CVD setup remained isolated from the outside atmosphere. The system was left at 475°C for about an hour, after which it was allowed to cool down to room temperature. The Ar flow through the quartz tube was maintained for the duration of the cooling process.

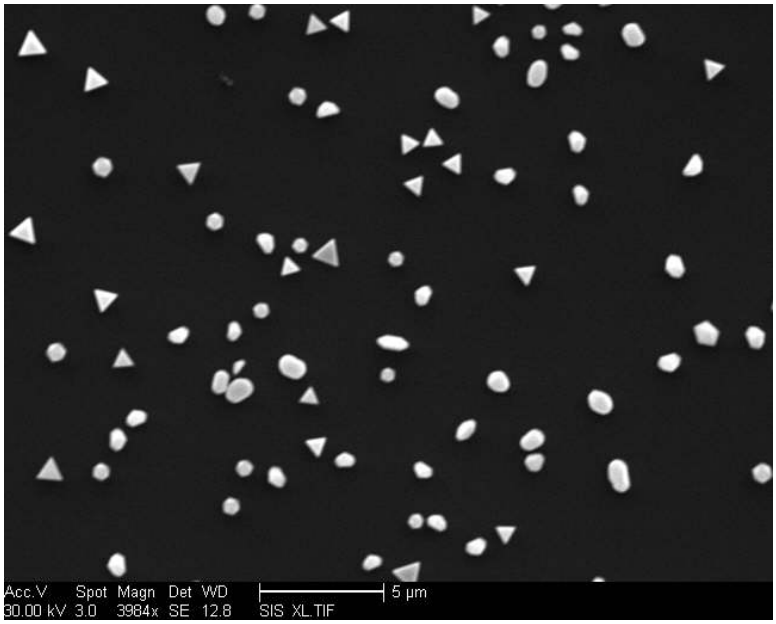

Figure 5.1: SEM image for gold nanocrystals. Gold nanocrystals grown using a catalyst-free thermal chemical vapor deposition (CVD) onto a Si (100) substrate.

5.3 Sample preparation

In this study, Au nanocrystals were grown using thermal chemical vapor deposition (CVD) onto a Si (100) substrate with the native oxide using a catalyst-free thermal approach with $AuCl_3$ as a precursor. Approximately 1.0 g of powdered $AuCl_3$ was loaded in a boat and placed within a quartz tube at the center of a Lindberg Blue furnace at $475°C$, where the silicon substrate still remains unoxidized because the oxidation of silicon is performed above $800°C$[61]. An Ar carrier gas was flowed through the quartz tubing while the downstream end of the CVD setup remained isolated from the outside atmosphere. The system was left at $475°C$ for about an hour, after which it was allowed to cool down to room temperature. The Ar flow through the quartz tube was maintained for the duration of the cooling process. Through this process, nanocrystals form in the absence of any foreign catalyst. In contrast, most synthesis techniques for Au nanocrystals employ surfactants to control shape or size. The roles of surfactants are widely reported. A growth mechanism is proposed linking both structural characteristic of the nanoparticles and the surfactants. A catalyst-assisted approach can be used to produce polyhedral shapes of nanocrystals and polyhedron with truncated corners/edges and also be involved in twinning growth of crystals. The shape control of gold nanocrystals can be done with the assistance of appropriate surfactants (e.g. cetyltrimethylammonium bromide (CTAB), cetyltrimethylammonium tosylate (CTAT), tetrabutylammonium bromide (TBAB), sodium dodecyl sulfate

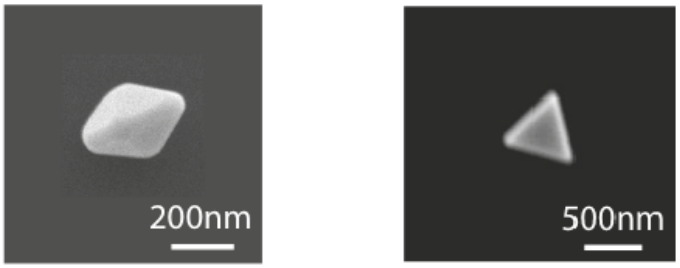

Figure 5.2: Octahedral and triangular-plate shaped gold nanocrystals in SEM image.

(SDS)) [62, 63, 64, 65]. These surfactants remain after the synthesis process is complete and can affect the physical properties of the nanocrystals. This synthesis method can be used to create many different shapes of gold nanocrystals, ranging from triangular plates, octahedra, and 26 faceted polyhedron to multiple twinned particles such as decahedra and icosahedra.

5.4 Coherent x-ray diffraction experiment

The coherent x-ray diffraction measurements were performed at Sector 34-ID-C of the Advanced Photon Source (APS) synchrotron facility. Figure 2.4 shows a schematic image of the setup we used for measurements of coherent x-ray diffractive imaging. An upstream monochromator was used to select E = 9.0 keV x-rays, which were focused onto the sample using Kirkpatrick-Baez mirrors that restricted the beam size to a region. The resulting diffraction patterns were measured using a charge-coupled device (CCD) with 22.5 pixels located along the detector arm at a distance of 0.9 m beyond the sample. The measured 2D diffraction patterns for a triangular nanoplate and an octahedral nanoparticle are shown in Fig. 5.2. These coherent diffraction patterns were recorded for the rocking curves of the (111) Bragg reflections by rotating the sample through the Bragg peak in increments of 0.005°. 121 frames were collected in this manner for each nanocrystal, covering a total angular range of 0.6°. Isosurfaces of the 3D diffraction patterns, obtained by stacking up the 2D diffraction data collected during rocking scans. The fringes, seen as spatial modulations in the signal, originate from the interference between waves diffracted from pairs of sharply terminated crystalline facets. Accordingly, the four pairs of fringe modulations in the diffraction pattern imply the presence of eight facets (i.e. an octahedron). The lack of inversion symmetry in the diffraction pattern reflects the strain in the nanocrystal [66].

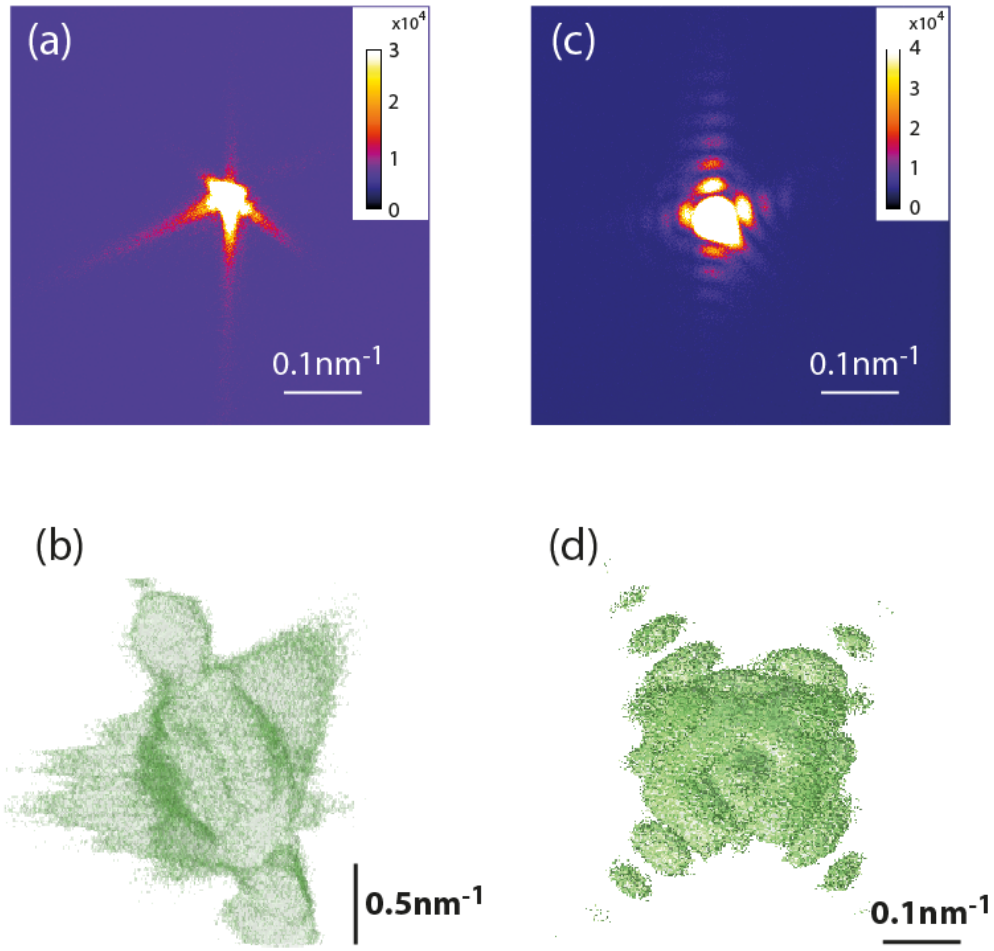

Figure 5.3: Measured 2D and 3D diffraction patterns from (111) Bragg reflections for triangular plate and octahedral gold nanocrystals. (a) and (c) measured 2D coherent x-ray diffraction patterns from (111) Bragg reflections for a triangular nanoplate and an octahedral gold nanoparticle, respectively, (b) and (d) 3D diffraction patterns for each particle obtained by rocking scans with a total 121 frames.

5.5 Phase retrieval procedure

The displacement field projected along the {111} Bragg plane direction was measured to quantify the internal nanoscale strain field within the nanocrystals. The missing phase of the diffracted wave was retrieved by using an iterative algorithm. The retrieval algorithm begins by taking a Fourier transformation of the amplitude from the measured diffraction pattern and coupling it with a random guess for the phase. The algorithm iterates back and forth between real and reciprocal space while applying constraints in every cycle [31, 32]. The real space constraints ensure that the amplitude, corresponding to the electron density, outside of the support, in which the object is assumed to exist is set to zero. In reciprocal space, the computed modulus is replaced with the square root of the measured intensity. Alternations of error reduction (ER) and hybrid input output (HIO) phase retrieval algorithms are applied [32]. In addition, the shrink-wrap algorithm is applied periodically to optimize the support as the algorithm progresses [41].

5.6 Results and discussion

These equilibrium nanocrystal shapes can be understood by employing the Wulff construction theorem [44]. We further studied the three-dimensional electron density, lattice displacement and strain distribution in these gold nanocrystals by using synchrotron-based coherent x-ray diffractive imaging [6]. In addition to

the nanocrystals enclosed by identical polygonal surfaces, plate-like flat crystals are also formed during synthesis. These plate-like structures exhibit a triangular morphology with basal surfaces bounded by two (111) facets and three (100) facets along the sides [58]. This shape is not explained by conventional thermodynamical arguments due to a relatively large surface area-to-volume ratio. However, it can be explained from the growth of a nanocrystal seed in the presence of a stacking fault [67]. If the planar seed exhibits a stacking fault, Au atoms added in close proximity to the fault give rise to crystal growth [67, 68]. Regardless of this difference in process of formation, gold nanocrystals with both triangular plate and octahedral shapes retain symmetries inherent to the fcc unit cell [69].

5.6.1 Octahedral nanocrystal

The geometry of gold nanocrystals on a silicon substrate with momentum transfer wave vector Q for the (111) Bragg reflection is shown in Fig 5. 4(a). Q is normal to the substrate for both crystals. Figure 5.4 (b) and (c) show the shapes of the reconstructed crystals. The top and bottom surface of the octahedral nanocrystal are identified by the same transformation of triangular plate, which has distinguishable top and bottom surface from the diffraction pattern to the object on the substrate in real space. The edge length of the octahedral nanocrystal is about 220 nm. The triangular plate has an edge length of about 600 nm and a thickness of about 60 nm. The phase (shown on the color scale) indicates a projection of the deformation onto the reciprocal lattice vector Q. Thus, the phase

is the deformation along the normal to the substrate surface in both nanocrystals. In the case of the triangular plate, due to the small thickness of a plate-like nanocrystal, area of contact with the substrate is so large that the physical deformation is closely associated with the direct interaction between a nanocrystal and its substrate. Two perpendicular cross-sectional planes, both containing the {111} Q vector were chosen for detailed analysis of displacement and strain distributions as shown in Fig 5.5(b). Figures 5.5 (c) and (d) show the phase shifts on the planes depicted in Fig 5.5(b). Both images clearly show that the displacements along the vertical direction, which corresponds to the {111} Qvector, occurred primarily near the surfaces. Moreover, the phase shifts near the top and bottom surfaces are colored blue (negative) and red (positive), respectively. This pattern indicates that the atoms near the top and bottom surfaces moved towards the center of nanocrystal. A distinct contraction of the surface layers of a gold nanocrystal has been confirmed by *Huang et al* in models of experimental diffraction patterns and molecular dynamics simulations [53].

The normal strain is generally defined as the derivative of the displacement, where is the normal strain along the x-direction. The 3D strain distribution of the entire volume along the {111} Qvector direction was obtained by taking the derivative of the displacement field resulting from algorithmic phase reconstruction. Figures 5.5 (e) and (f) show the perpendicular slices that represent strain fields on the planes depicted in Fig 5.5 (b). The concentration of compressive strain in particular regions, as well as the overall inward contraction, is readily apparent.

Strong compressive strains are located mainly at the vertices or edges, whereas the weaker strain distribution appears on the flat surfaces. The center of the crystal remains nearly strain-free. This observation is in good agreement with recent studies of strain distribution in metal nanocrystals. These studies found evidence of compressive strain under the locally rounded surface regions of metallic nanocrystals where (111) planes intersect, and exhibit relatively less compressive strain near flat surface regions [70, 71].

We observed that the strain near the bottom surface of the octahedral nanocrystal is significantly stronger than that near the top surface. The measured strain is -4.2×10^{-4} and -5.0×10^{-4} near the top and bottom surfaces, respectively, as in Fig 5.5 (e). The phase-retrieval real space density distribution is well-known to have a two-fold degeneracy because the combination of inversion symmetry and complex conjugate to any complex function solution is also a solution, resulting in identical experimental data [33]. Therefore, while Figure. 5.5(e) and (f) show an octahedron with greater compressive strain at the bottom facet based on diffraction data alone, it is not possible to completely rule out an inversion symmetry, equivalent solution where the top facet is unusually strained instead. However, we postulate that it is much more likely that the bottom facet has the greater compressive strain, since such orientation of octahedron (see Fig 5.5(e) and (f)) would be consistent with the strain induced by the underlying substrate, whereas the top facet solution lacks any clear explanation for such substantial strain modification. This assumption is further supported by greater compressive strain induced by

the substrate also observed in triangular nanoparticles, a case in which the correct orientation can be determined from independent SEM measurement. The strain on the rounded surface of a particle of radius R can be estimated quantitatively by the Young-Laplace equation for a given bulk modulus K of the material. Surface stress results in a pressure difference between the inside and outside regions of a material that effectively compresses an isotropic particle. For a lattice constant of a:

$$\frac{\Delta a}{a} = -\frac{2\sigma_s}{3KR} \tag{5.1}$$

Surface stresses for metals are usually tensile in nature, in the range of 2N/m [48, 49]. The bulk modulus of gold is 180 GPa and the radius of the locally rounded region is 18 nm in the upper right portion of Fig 5.5 (e). According to Eq. (5.1), the strain under the rounded surface should be -4.1×10^{-4}. This value is in good agreement with the measured strain of -4.2×10^{-4}. However, the strain at the bottom surface is approximately 20 % higher than that at the top surface. In general, inhomogeneous internal strain in nanocrystals can be caused by irregular surface relaxations [72]. Surface stress, which is coupled with internal strain, depends on the chemical composition of the surface and its interfaces with neighboring particles, substrates, solvents, surfactants, etc [71]. In our experimental environments, the irregular relaxations at the surfaces may be attributed to the dissimilarity in interfacial energies at the substrate. The different surface en-

ergies at Au/Air and Au/Si interfaces determine an internal strain accumulation during the growth of a nanocrystal [73]. Furthermore, when the nanocrystals are cooled down to room temperature, the strain at the interface is induced by the difference in the thermal expansion coefficients between the Au nanocrystals and the Si substrate.

Within the temperature range of the synthesis process, the thermal expansion coefficient of Au, $\alpha_{Au} = 1.4 \times 10^{-5} K^{-1}$, is greater than that of Si, $\alpha_{Si} = 0.3 \times 10^{-5} K^{-1}$. As a result, the Au nanocrystal contracts more than the Si substrate as they are cooled down. Therefore, compressive strain fields along the Qvector are induced by the tension along the bottom surface, which is parallel to the substrate surface. As shown in Fig 5.5 (e) and (f), these compressive strains are not distributed uniformly across the bottom surface. This distribution can be attributed to a partial relaxation of the strain due to an incomplete contact between the nanoparticle and the substrate surface. Since strain is calculated with respect to the normal direction of the substrate surface, the strain distribution at the right and left sides of Fig 5.5 (e) and (f) lie nearly in-plane, while the strain distribution in other regions show out-of-plane components. Most metal surfaces exhibit tensile surface stress because they tend to reduce interatomic distances in surface planes [49]. Accordingly we are seeing the signature of tensile surface strain in the octahedral nanocrystals.

Table 5.1: The coefficients of linear thermal expansion (α)

α	Au	Si
$10^{-6}/K$	14.3	3

Table 5.2: The comparison of strains

Strain	Young-Laplace equation	Reconstruction
$\times 10^{-4}$	-4.1	-4.2

Table 5.3: The maximum compressive strain values at top and bottom

Strain	Top	Bottom
$\times 10^{-4}$	-4.2	-5.0

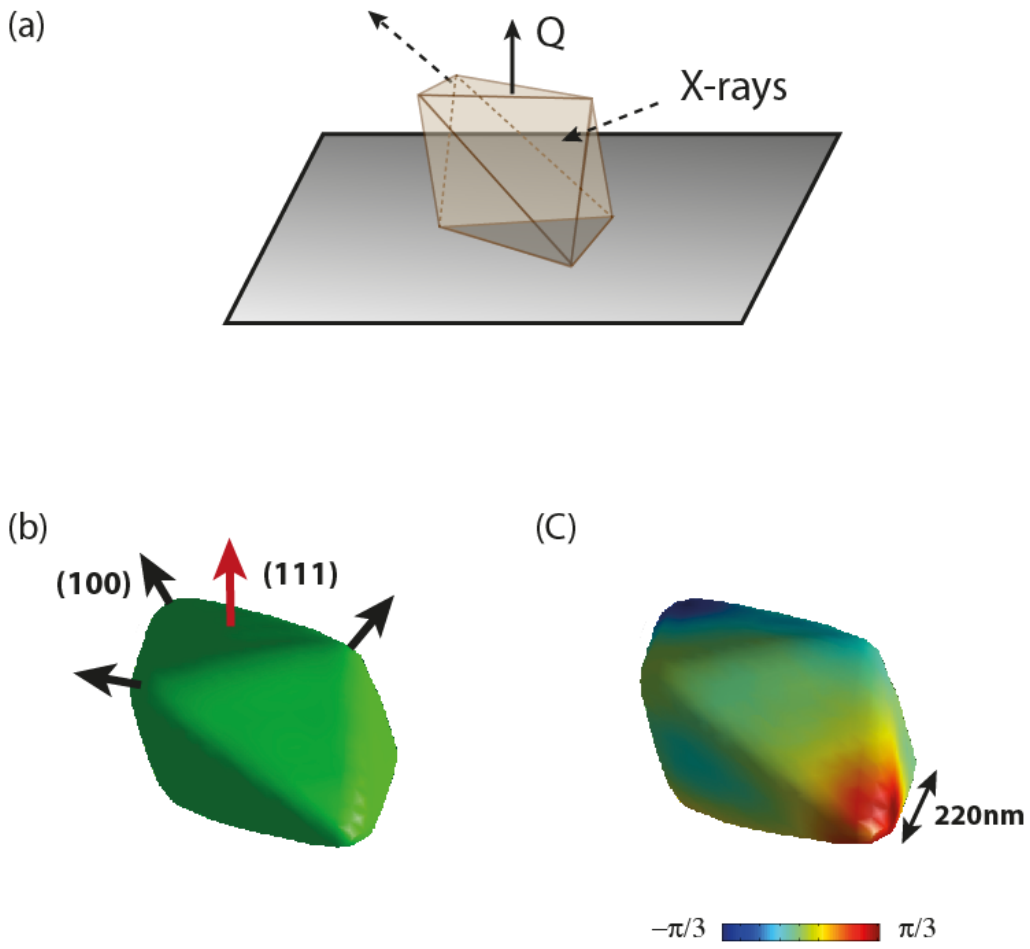

Figure 5.4: The geometry of octahedral gold nanocrystal with momentum transfer vector and results of reconstruction. (a) The geometry of gold nanocrystals on a silicon substrate. The momentum transfer wave vector Q for the (111) Bragg reflection is oriented normal to the substrate. (b) Isosurfaces of the reconstructed shape for an octahedral nanoparticle. The normal directions of two sets of crystalline planes (111) and (100) are marked by red and black arrows, respectively. (c) The color represents the local value of the phase at the surface, indicating the presence of strain.

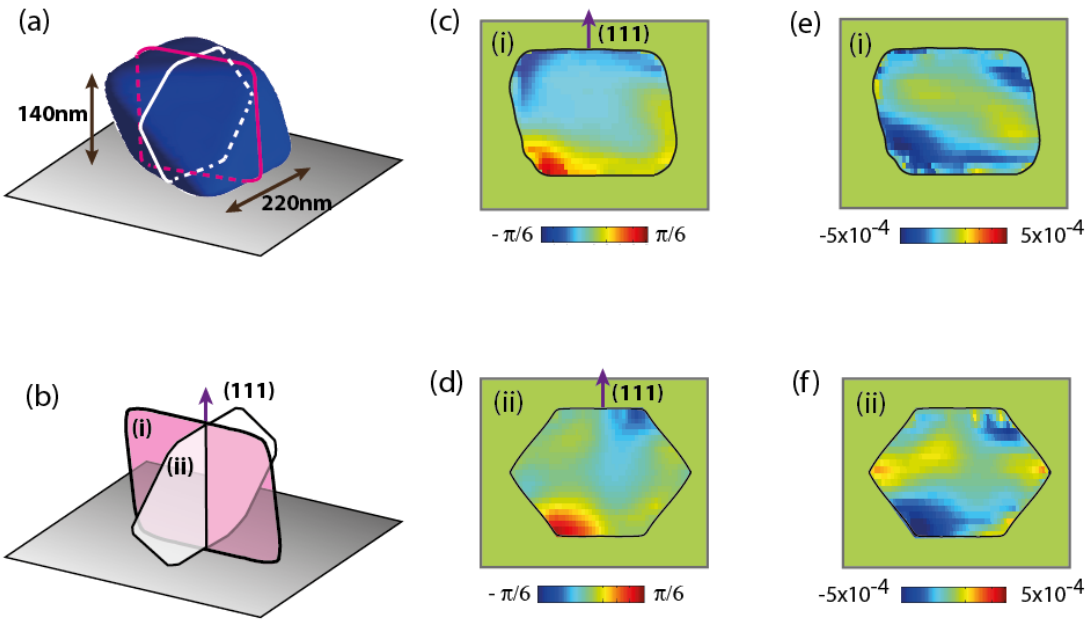

Figure 5.5: The phase and strain distribution on two cross-sections inside octahedral gold nanocrystal. (a) The geometry of the nanocrystal and outlines of two cross-sections, (b) which are perpendicular to the bottom surface, and contain the {111} Q vector. 2D phases on the cross-sections, depicted in (b), are shown in (c) and (d). Strain fields, calculated by the gradient of the displacement on plane (i) and (ii), are shown (e) and (f), respectively.

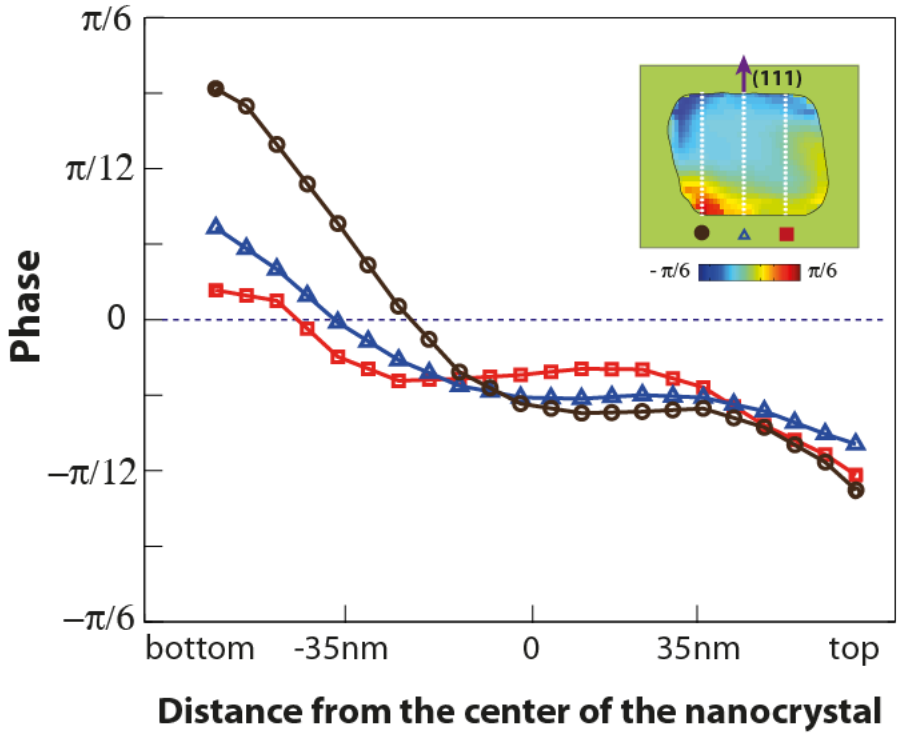

Figure 5.6: The plot of phases on a slice of a octahedral gold nanocrystal. Three line scans of phases along the plane of the inset. Brown, blue, and red lines represent phases along the left, center, and right white dashed line, respectively in the inset.

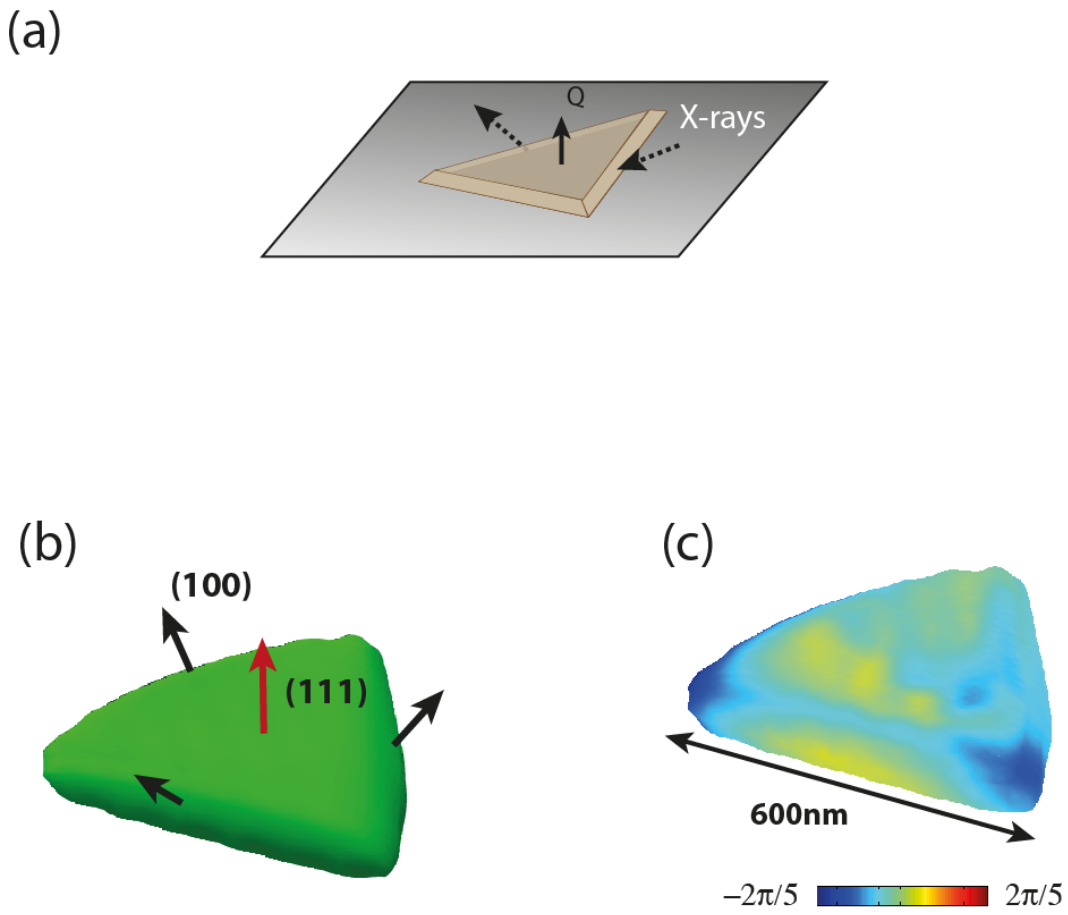

Figure 5.7: The geometry of triangular plate gold nanocrystal with momentum transfer vector and results of reconstruction. (a) The geometry of gold nanocrystals on a silicon substrate. The momentum transfer wave vector Q for the (111) Bragg reflection is oriented normal to the substrate. (b) Isosurfaces of the reconstructed shape for a triangular plate nanoparticle. The normal directions of two sets of crystalline planes (111) and (100) are marked by red and black arrows, respectively. (c) The color represents the local value of the phase at the surface, indicating the presence of strain.

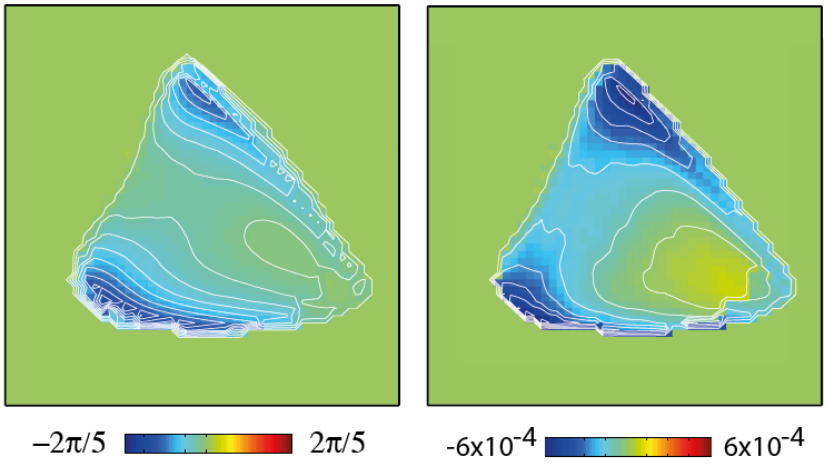

Figure 5.8: Averaged phase and strain of triangular plate gold nanocrystal. (a) and (b) Phase and strain along the normal to the basal plane of the triangular nanoplate, averaged over the depth.

5.6.2 Triangular plate nanocrystal

Figures 5.8 represent phases and strains, respectively, averaged over the depth of the triangular plate. A primarily negative distribution of phases shows that the triangular plate deformed downwards. The compressive strain along the Q vector is induced in much the same way as the compressive strain near the bottom of the octahedral nanocrystal, as discussed in the preceding paragraph. The height-to-length ratio of the triangular plate is so small that the displacement of the entire volume is affected predominantly by the difference in thermal expansion between the nanocrystal and the substrate. Figure 5.9 shows the distinct strain distribution at top and bottom surfaces. The fact that there is more compressive strain at the bottom surface compared to the top surface is consistent with the strain distribution of octahedral nanocrystals as shown in the table 5.3.

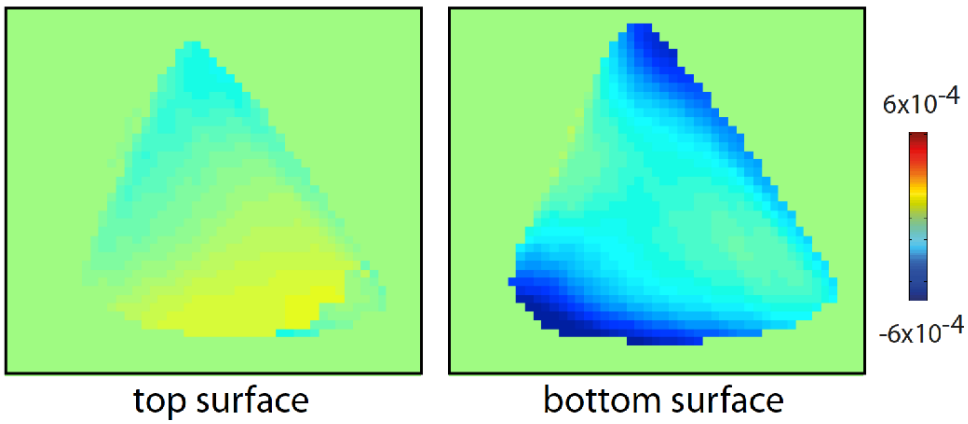

Figure 5.9: Strain distribution of triangular plate at top and bottom surfaces.

5.6.3 A 26 faceted polyhedral nanocrystal

We have found a 26 faceted polyhedral nanocrystal and reconstructed it as shown in Fig 5.10. This polyhedral nanocrystal is surrounded and bound by the six (100), twelve (110), and eight (111) facets. It was found that the gold nanocrystals were transformed from rhombic dodecahedron to octahedron enclosed by the most stable (111) facets via 26 faceted polyhedron driven by the concentration of PVP (poly-vinylpyrrolidone) and the water content [74]. In lithium ion storage, ferroferric oxide, Fe_3O_4, appears as not only 26 facted form of nanoparticle, but also 14 faceted truncated octahedron containing six (111) and eight (111) facets [75]. This gold nanocrystal could be an intermediate state in the process of shape evolution.

Because of this particular shape, which has O_h symmetry same as octahedral nanocrystal, it is not possible to assign top and bottom facets since the solution of phase retrieval has essentially inversion symmetry. However, this problem can be overcame with the help of *prior* knowledge. The facet that contacts with the substrate surface can be identified based on the fact that the atoms near the top and bottom surfaces moved towards the center of nanocrystal [53]. In our study, one of (100) or (111) facets of 26 faceted polyhedron gold nanocrystal is likely on the substrate surface. This is also consistent with the strain distribution of octahedral and triangular plate gold nanocrystals as discussed in the preceding sections.

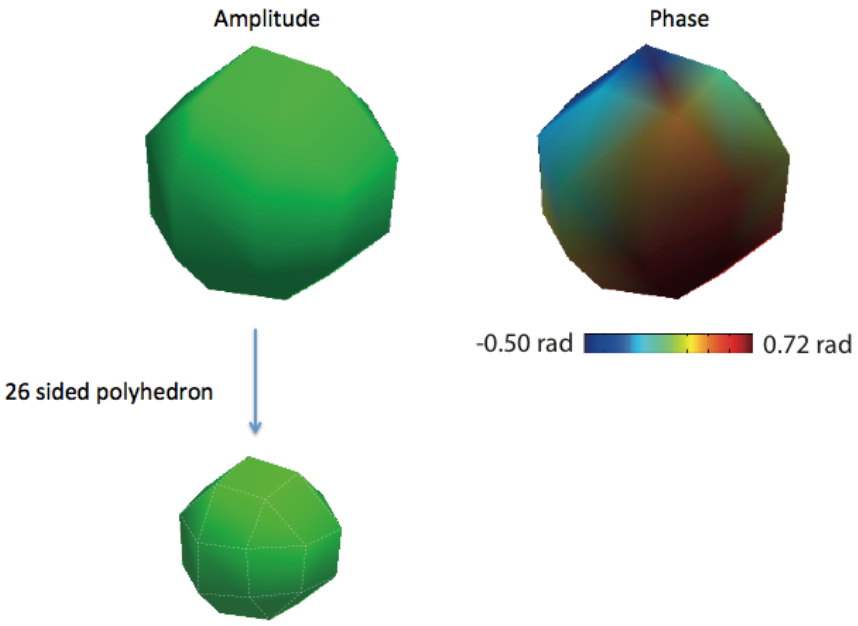

Figure 5.10: The reconstructed amplitude and phase of the 26 faceted polyhedron nanocrystal.

5.7 Inversion symmetry

It is important to identify sign of the displacement of the nanocrystals since the diffraction is inherently centrosymmetric with all measured intensity. So the complex density image, $\rho(r)$, obtained from mathematical inversion of the measurement is indistinguishable from $\rho^*(-r)$, which is a complex conjugate. The solution results from the phasing algorithm can be one of the two solutions, which is arbitrarily determined. Therefore, if the nanocrystal has 2-fold symmetry, it is not possible to find 'true' solution using the measurement data, which is diffraction pattern itself.

For the triangular plate gold nanocrystal, the inversion symmetry can be ruled out based on comparison with SEM image as shown in Fig 5.11. The phase and strain distributions of this nanocrystal (see Fig 5.8 and 5.9) indicate that there are more compressive strain at the interfacial surface with the substrate. This result of phase retrieval implies that the strain distribution of the surface adjacent to substrate is affected by the substrate significantly. We can find a 'true' direction of displacement for the other nanocrystals such as octahedron and 26 faceted polyhedron gold nanocrystal in such a way that the strain distributions are consistent with those of triangular plate, which is known. So we were able to identify top and bottom surfaces for these two nanocrystals. We can avoid the inversion symmetry with the help of *prior* knowledge such as other images or evident results.

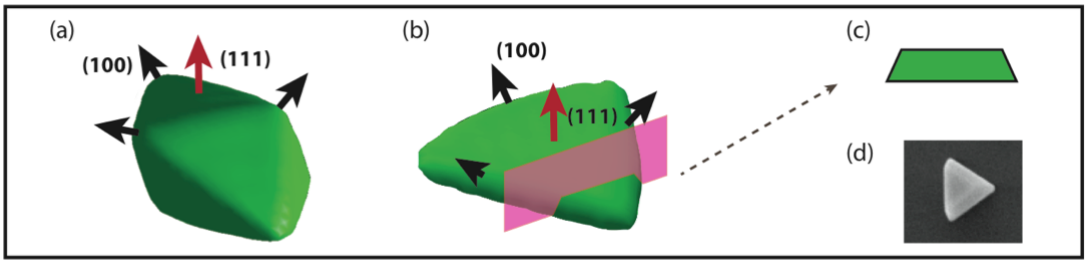

Figure 5.11: Identification of inversion symmetry. For triangular plate, inversion symmetry can be rule out based on the comparison with SEM image. The study of internal structure of triangular plate helps the identification of inversion symmetry for octahedral gold nanocrystal, which is not possible using diffraction data alone.

5.8 Conclusion

In conclusion, we have observed the atomic-level structures and internal strain distributions in Au nanocrystals with the morphology of an octahedron, triangular plate, and 26 faceted polyhedron grown by CVD at a temperature of $475°C$. Phase reconstruction reveals the lattice distortion of the three nanocrystals along the {111} direction. In the octahedral nanocrystal, it is observed that there is a contraction of the lattice near the surfaces, accompanied by a compressive strain beneath these surfaces, especially near locally rounded surface regions. The strain on the surface of these rounded regions is in good accordance with theoretical predictions from the Young-Laplace equation. However, the strain near the bottom surface shows a discrepancy. We conclude that this inhomogeneous internal strain distribution is caused not only by the dissimilar surface energies of the interfaces during the growth process, but also by differing thermal expansions between gold nanocrystals and the silicon substrate when they are cooled down to room temperature. In the case of a thin nanoplate crystal, the difference in thermal expansion is the primary contributor to the strain fields of the entire particle. The 26 faceted polyhedral gold nanocrystal, which is likely intermediate state of shape evolution, has shown the same tendency of strain distribution with octahedral nanocrystal. This is the first study of both curvature-induced strain under a locally rounded surface and thermal strain at the nanocrystal-substrate interface in a single Au nanocrystal.

Chapter 5, in full, is a reprint of the material "Curvature-induced and thermal strain in polyhedral gold nanocrystals" as it appears in the Applied Physics Letters, Jong Woo Kim, Sohini Manna, Sebastian H. Dietze, Andrew Ulvestad, Ross Harder, Edwin Fohtung, Eric E. Fullerton and Oleg G. Shpyrko, 2014, 105, 173108. The dissertation author was the primary investigator and author of this paper.

Chapter 6

Radiation pressure on nanocrystals

Coherent x-ray diffraction imaging is a powerful technique that can be used to explore the internal structure of nanoscale objects. When a coherent x-ray beam is incident on and scattered by an object, a diffraction pattern appears in the far field. These diffraction patterns can be collected on a 2D detector within a certain range of incident angles and combined to obtain a 3D diffraction pattern. During this process, the integrated intensity can be described by a bell-shaped distribution. However, we observed that the Bragg peak from a Ni nanowire abruptly shifted in the middle of rocking scan without a drop of intensity. We demonstrated that this phenomenon can be attributed to radiation pressure on the nanowire. Having ruled out motion due to thermal effects on the sample and the substrate, we revealed that the nanocrystal was pushed by x-ray radiation pressure.

6.1 Introduction

Third generation synchrotron facilities provide brilliant x-ray beams with a very high degree of coherence and high flux, allowing researchers to make great advances in the study of nanostructures [7, 54]. Bragg coherent x-ray diffraction, combined with computational phase retrieval techniques, has proven useful for understanding the structure of nanocrystalline materials [71]. When a sample is exposed to monochromatic x-ray radiation, the x-rays scatter from different regions of the sample and interfere constructively or destructively at angles that fulfill a particular relationship set by the Bragg equation. Three-dimensional diffraction patterns in the far field can be comprised from an appropriately collected set of 2D diffraction patterns via a technique known as a rocking scan. In a rocking scan, the sample is rotated relative to the incident x-ray beam such that the entire volume of the sample can be illuminated by the beam at slightly different angles. A mathematical inversion of the 3D diffraction pattern results in a complex-valued density function. The amplitude of this complex function is proportional to the electron density in the crystal, while the phase can be interpreted as the deformation of the lattice as projected onto the momentum transfer vector [59]. This technique relies on the fact that the x-ray beam is non-destructive so that the location of sample and its properties are not altered during the measurement. Some biological samples and protein crystals, however, can be damaged or even destroyed by an x-ray beam [76]. This radiation damage has been acknowledged

as major problem in x-ray science, resulting in a rigorous study of the minimum dose required to produce an image with a given resolution [77, 78, 79]. However, inorganic materials have higher radiation tolerance and are largely invulnerable to synchrotron x-ray radiation.

The x-ray radiation pressure was measured using diffracted x-ray tracking of gold nanocrystals, which are designed to be linked to a substrate with a filament [80]. However, we present here some intriguing data that we obtained while performing a Bragg coherent x-ray diffraction experiment to study the internal structure of nanowires. We observed a substantial shift in the Bragg peak while monitoring a 2D diffraction pattern. This fact is indicative that something undesirable occurred in the sample or its environment during the experiment, resulting in an unsuccessful collection of 3D diffraction data. It is necessary to investigate this phenomenon in order to determine appropriate corrections for Bragg coherent x-ray diffractive imaging.

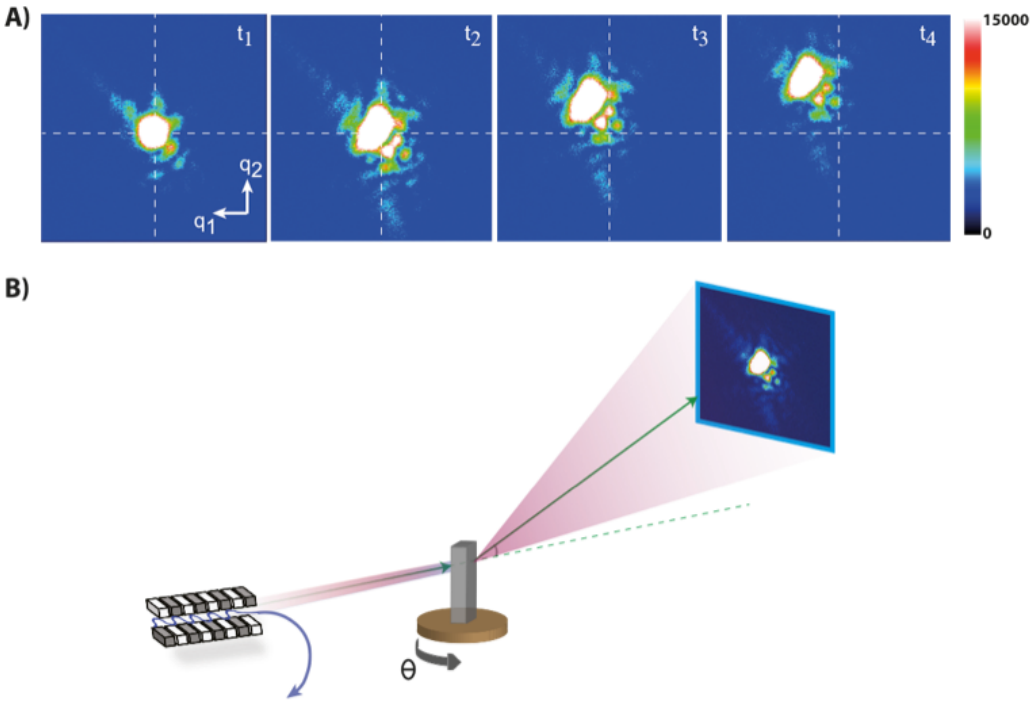

Figure 6.1: (a) A series of 2D diffraction patterns collected during a rocking scan. 51 frames of 2D diffraction patterns were collected over a time period of 51 minutes. The four images are selected at t_1 (35^{th} min), t_2 (40^{th} min), t_3 (45^{th} min), and t_4 (50^{th} min), respectively. (b) The experimental setup. The incident and diffracted beam angles are chosen to produce an intense peak, which is the Bragg peak. The theta motor rotates by 0.01° incrementally.

6.2 Experiment

Ni nanowires were grown vertically on a silicon substrate using chemical vapor deposition (CVD) technique [52]. These nanowires exhibited a large height-to-width ratio with a height 2 μm and a width of 200 nm. They took the form of an inverted pyramidal structure at the bottom portion, so that the sample looked like a long nanowire with tapered base. Coherent x-ray diffraction measurements were performed at beamline 34-ID-C of the Advanced Photon Source at Argonne National Laboratory, with an x-ray energy of 9 keV selected by a monochromator. The coherent beam was then focused with horizontal and vertical Kirkpatrick-Baez mirrors to a size of about 1.5 μm in both directions.

The off-specular (111) Bragg plane direction of Ni nanowires was chosen for coherent x-ray diffraction measurements. The x-ray beam illuminated the Ni nanowire on the silicon substrate and the far-field diffraction intensity was measured by a charged coupled device (CCD) detector with 22.5 μm pixels, placed 0.5 m away from the sample. A 3D diffraction pattern was measured around the Ni (111) Bragg peak as a function of the wave transfer vector $Q = k_f - k_i$, where k_i is the incident wave vector and k_f is a diffracted wave vector. The measured reciprocal space positions are given by $q = Q - G_{111}$ around the (111) reflection (Bragg vector G_{111}) with the components $q_{1,2}$ lying in the detector plane, vertically and horizontally, respectively [81].

The q_θ component is the offset from the Bragg angle. It is perpendicular to

both in-plane components q_1 and q_2, and increases linearly with the motor angle θ, which is responsible for the rotation of the sample:

$$\Delta q_\theta = \frac{2\pi}{d_{111}} \times \Delta\theta \tag{6.1}$$

where Δq_θ is the reciprocal space unit vector in the θ (rocking) direction, d_{111} is the lattice constant of the nickel (111) direction [82]. The component q_θ increases linearly over the scanning time so that the entire 3D diffraction pattern can be obtained. The distribution of integrated intensities is a normally bell-shape along q_θ direction. Figure 6.1 (a) shows a series of measured 2D diffraction patterns during a rocking scan. The sample was rocked within a range of $\pm 0.25^\circ$ in 0.01° increment. The angle was incremented every minute so that the rocking scan consists of 51 frames and 51 minutes in total.

Figure 6.2 (a) shows the 3D diffraction pattern obtained by stacking up 51 2D diffraction patterns along q_θ direction, which is equivalent to time frame. Figure 6.2 (b) represents four contours extracted from corresponding 2D diffraction patterns shown as Fig 6.2 (a). The fact that the 3D diffraction pattern is bent and the four contours look almost same indicates that the center of the Bragg peak started to shift along a particular direction in the middle of the rocking scan and the 2D diffraction patterns are maintained within the detector area during the entire scan time. The Bragg peak shifts by 100 pixels on the CCD detector, which is equivalent to a 0.2 nm^{-1} shift in reciprocal space.

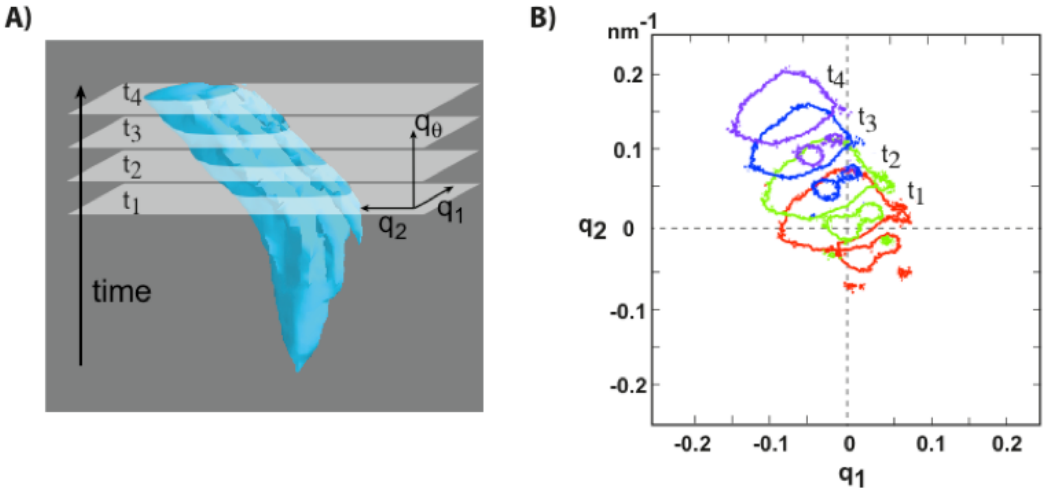

Figure 6.2: (a) 3D diffraction is obtained by stacking up 2D diffraction patterns. The four slices represent four 2D diffraction patterns measured at different times shown as Fig 6.1(a). (b) Four contours are extracted from each 2D diffraction pattern measured at at t_1, t_2, t_3, and t_4 shown as (a). The origin point (0,0) is defined as the spot where the Bragg peak starts to shift.

6.3 Results and discussion

To analyze the Bragg reflections along the q_θ direction, the curves at each 2D diffraction pattern was fitted to a Gaussian and the position of the brightest spots were extracted. This quantity is plotted versus time in Fig. 6.3 (a). After some initial variation, there is a roughly linear increase in the Bragg peak shift after t=35 minutes, which is defined as t_1. During this period, the 2D diffraction patterns are maintained, as shown in Fig 6.3 (b).

$$h(m,n) = \frac{\sum_{k,l}(I_{t_1}(k,l) - \overline{I}_{t_1})(I_x(m-k,n-l) - \overline{I}_{x^{th}(m,n)})}{(\sum_{k,l}(I_{t_1}(k,l) - \overline{I}_{t_1})^2 \sum_{k,l}(I_x(m-k,n-l) - \overline{I}_{x^{th}(m,n)})^2)^{0.5}} \tag{6.2}$$

wehre $h(m,n)$ a normalized cross correlation function, I_{t_1} a diffraction intensity at time t_1 and I_x a diffraction intensity at the x^{th} frame. Normalized cross correlations are calculated between the 2D diffraction intensities and the intensity measured at time t_1, where the Bragg peak starts to shift. The maximum values are extracted from each function and plotted as a function of time. This value represents the similarity of the diffraction pattern with the one measured at the time t_1. It decreases just by 2.3% since the time t_1

Typically, the from of 2D diffraction pattern changes during the rocking scan because its shape is determined by the part of the Ewald sphere in reciprocal space that is rotated through a particular angle of the sample with respect to incident beam. In addition, the diffraction intensity typically drops to the level of noise at the end of rocking scan. However, Figure 6.3 indicates that undesirable effects such as an abnormal rotation of the Bragg plane (111) occurred, since the Bragg peak shifts without decay of intensity, which is not expected during the rocking scan.

There are no other factors than x-ray radiation that can influence both the sample and the substrate during a rocking scan unless the experimental devices touch the sample. X-ray radiation can deliver photon energy to the sample and/or its substrate. It can also exert radiation pressure on the sample. In the following paragraphs, we present our evidence that x-ray radiation pressure caused the Bragg peak to shift during this rocking scan.

As the temperature of a Ni nanowire increases, the vibration of atoms in

a lattice around their equilibrium position increases so that the overall diffraction intensity decreases by Debye-Waller factor without a spatial shift of the Bragg peak [83]. FFurther increase of temperature can expand d-spacing, which is the distance between adjacent atomic Bragg planes, in such a way that the Bragg peak moves out of the Debye-Scherrer (D-S) ring, whose radius depends on the lattice constant. In our experiment, however, it was observed that the Bragg peak consistently sits on the D-S ring, around which it rotates by an angle of $0.4°$. This evidence indicates that the thermal effect of x-ray radiation on the sample is not the cause of the Bragg peak shift. If the substrate was deformed by a thermally-induced strain due to x-ray radiation, a tilt of the Ni nanowire can occur leading to a shift of the Bragg peak. The estimate of the temperature increase that could be caused by x-ray radiation in a substrate based on heat transfer analysis is less than 1K even without taking heat loss due to natural convection into account. For this estimation, we have assumed that the entire photon energy is absorbed and converted to heat on the substrate surface over the illuminated beam foot-print. An overall x-ray power of $1.44 \times 10^{-6} W$ results from the calculation with a photon energy 9 keV at a rate of $10^9 photons/s$. We can thus conclude that the x-ray radiation plays a negligible role in raising the temperature of the substrate and therefore, the thermal effect on the both sample and substrate is insignificant.

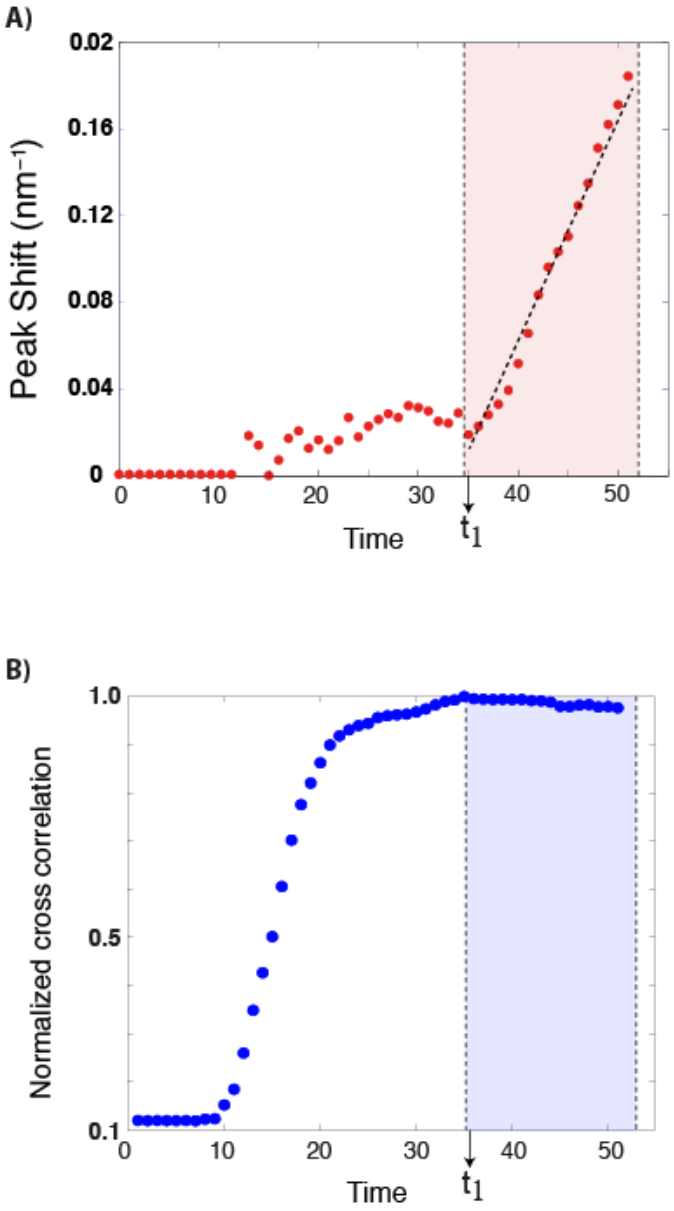

Figure 6.3: (a) Position of the (111) Bragg peak versus time. The peaks were fitted to a Gaussian to extract the position. There is a variation of peak shift followed by a roughly linear increase of peak position in time. (b) The normalized cross correlation of the 2D diffraction intensities with the 2D diffraction intensity measured at t_1 (35^{th} min).

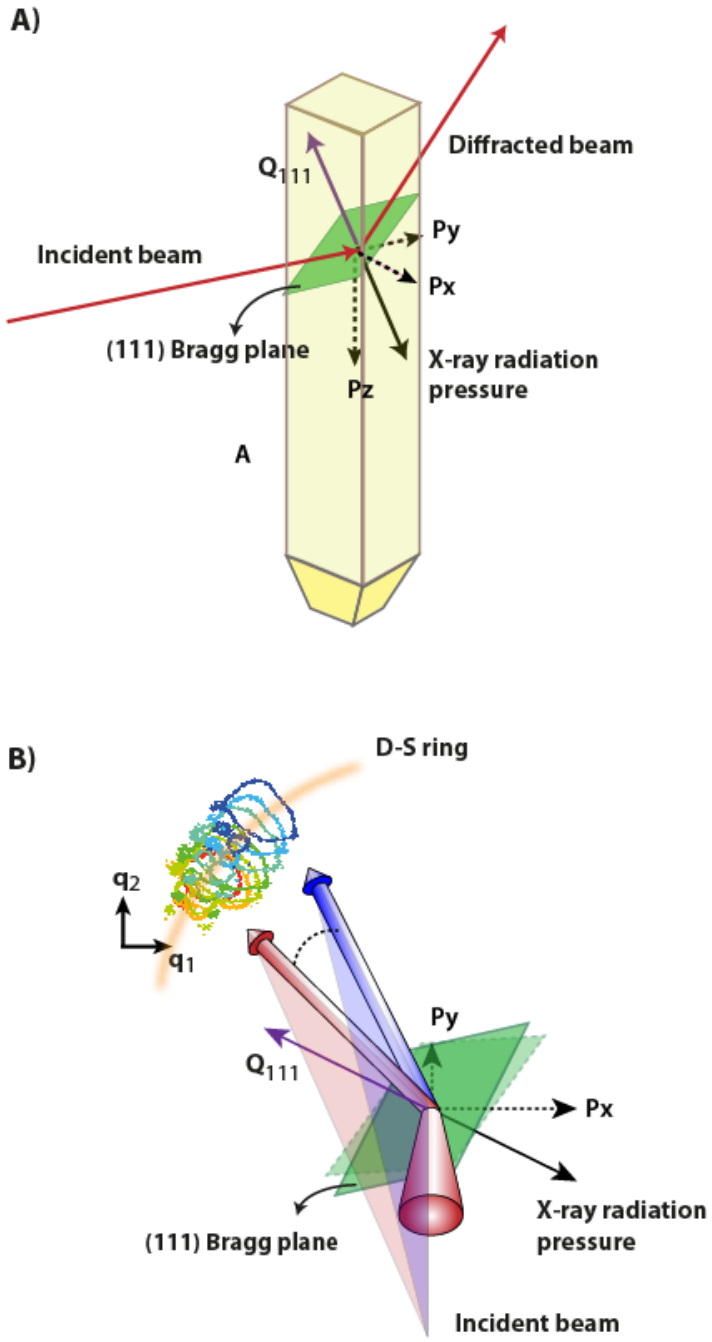

Figure 6.4: (a) Incident x-ray beam diffracts from the (111) Bragg plane. The direction of x-ray radiation pressure is determined by the opposite to the transfer wave vector. It is decomposed into three vectors P_x, P_y, and P_z. (b) The pressure vector P_x is responsible for shift of the Bragg peak and the pressure vector P_y forces the Bragg peak to move away from a detector plane.

We can evaluate the movement of the Bragg peak based on the assumption that the Bragg reflection plane was pushed by x-ray radiation pressure. The geometrical analysis was performed in a Cartesian coordinate system, The y-axis is defined parallel to the incident beam and the z-axis is normal to the ground, while the x-axis is orthogonal to both the y and z-axes (see Fig 6.4 (a)). The direction of the x-ray radiation pressure is opposite to the wave transfer vector. If the Bragg plane of the Ni nanowire was pushed towards the direction in which the radiation pressure was applied, the sample would tilt accordingly. The radiation pressure can be decomposed into three vectors with respect to x, y, and z directions. The pressure P_x and P_y can make the (111) Bragg reflection plane tilt along x- and y-direction, respectively. The tile of (111) Bragg reflection plane along x-direction can cause the Bragg peak to shift on D-S ring, which is transverse movement and the tilt along y-direction can move the Bragg peak away from a detector plane, which is longitudinal movement. The transverse movement of the Bragg peak is consistent with our observation, the shift of the Bragg peak as shown in Fig 6.4 (b). However, the Bragg peak does not seem to move in a longitudinal direction because the diffraction intensity does not decay, but rather is maintained. Regardless of the x-ray radiation pressure, the rocking scan should inherently make the Bragg peak move away or come closer to the detector plane so that the 2D diffraction pattern disappears by the end of the end. Thus, the longitudinal movement of the Bragg peak that resulted from x-ray radiation pressure can be canceled out by the angular rotation of the rocking scan.

If the (111) Bragg reflection plane rotates around y-axis R_y by the angle that the Bragg peak shifts on the detector, which is 0.40°, the Bragg plane would rotate around x-axis R_x by $-0.18°$ based on the ratio of radiation pressure vector components P_x and P_y. The θ motor rotates by 0.15° during the shift of the Bragg peak between the beginning t_1 and the end. This rotation contributes to the rotation of the Bragg plane around x-axis by 0.19°, which is the almost same magnitude, but the opposite direction with the rotation caused by radiation pressure. Thus, the longitudinal movement of the Bragg peak can be canceled out by the rocking scan. As a result, x-ray radiation pressure can cause the Bragg peak shift along D-S ring direction while keeping the 2D diffraction pattern from changing shape or intensity.

Therefore, the postulation that the rotation of the Bragg plane results from x-ray radiation pressure is consistent with our observations of Bragg peak shift without change of the overall 2D diffraction pattern. In addition, the Bragg peak disappeared as soon as the rocking scan was finished. This represents that the Ni nanowire did not exist any more in the region where the x-ray beam passed through because the θ motor returned to the original position automatically and illuminated the sample right after the rocking scan was done. The Ni nanowire may be down after the rocking scan.

The x-ray radiation pressure on the Ni nanowire can be calculated by the following equation.

$$P_{rad} = \frac{\langle S \rangle}{c} \tag{6.3}$$

where $\langle S \rangle$ is a power flux density which is defined as the photon energy per unit time per unit area, and c is the speed of light. In this study, the photon energy was $9keV$ with a flux of 10^9 photons/s and the contribution of the photons on the x-ray radiation is about 0.5% because most of photons pass through the sample. Thus, the radiation pressure P_{rad} turns out to be approximately $2.4 \times 10^{-5} Pa$. According to the study of x-ray radiation pressure force, it was revealed that the force resulted from x-ray radiation at 10KeV is 0.33aN [80].

This tiny force is not enough to bend nor break normal Ni nanowire because the fracture strength of the same-sized nanowire is about 10 GPa [84]. Ni nanowire was likely standing or weakly attached on the substrate. The nanowire was pushed by radiation pressure and fell down on the substrate. This is supported by the facts that the Bragg peak disappeared following the rocking scan and the base of the nanowire is likely the weakest region because it is tapered at the bottom and stress would be concentrated on it. The shift of Bragg peak is rarely observed during rocking scan. This indicates that the radiation pressure force is generally not enough to exceed the normal fracture strength or adhesion of Ni nanowire to its substrate. The sample in which we observed the shift of Bragg peak may have contained a defect such that it was easily pushed by even a tiny x-ray radiation pressure.

In summary, we have observed the abnormal 3D diffraction patterns during the rocking scan for a Ni nanowire. This intriguing data results from the effect of x-ray radiation pressure on the samples. X-ray radiation inherently carries energy, the pressure of which can cause a sample to move if it exceeds the adhesion strength between the sample and a substrate. As a sample size gets smaller and photon flux increases, the x-ray radiation pressure on a sample has to be taken into account for hard x-ray scattering at synchrotrons.

Chapter 6, in full is currently being prepared for submission for publication of the material "Observation of x-ray radiation pressure on a Ni nanowire". Jong Woo Kim, Edwin Fohtung, Sohini Manna, Ross Harder, Andrej Singer, Leandra Boucheron, Eric E. Fullerton, Oleg G. Shpyrko. The dissertation author was the primary investigator and author of this paper.

Appendix A

Strain in elasticity

A strain is one of fundamental concepts from the mechanics of materials. It is a normalized measure of deformation representing the displacement between particles in the body relative to a reference length. The understanding and management of strain is of fundamental importance in the design and implementation of materials.

Let us consider now a cubic crystal with the elementary volume $dV = dx_i dx_j dx_k$ centered in a stressed material. The direction of x_k is defined as normal to the plane that the other two components make x_{ij}. The stress tensor is defined as a force per unit area σ_{ik}, where $i = 1, 2, 3$. If $i = k$, the force is applied normally to the i^{th} face, otherwise the shear stress is applied to the k^{th} face. The tensor σ consists of a total of 9 elements.

For mechanical equilibrium maintained under external forces f_i applied to the crystal, excluding torsion and/or rotation, we get the following condition

$$\frac{\partial \sigma_{ij}}{\partial x_j} = f_i \tag{A.1}$$

The notation is employed to define tensor components and associated operations with tensors. The sum is performed on the repeated indices using the notation. When the stress is applied on a crystal, the deformation can be observed. In the x, y, z coordinates, r is the radial vector that points each atomic position in the volume. The displacement field $u(r)$ is defined as follows:

$$r^{'} = r + u(r) \tag{A.2}$$

where r is the original vector in the case of an unstressed crystal and $r^{'}$ is current vector under the deformation. Thus, the strain can be introduced as follows:

$$\epsilon_{ij} = \frac{1}{2}\left(\frac{\partial u_i}{\partial x_j} + \frac{\partial u_j}{\partial x_i}\right) \tag{A.3}$$

The strain defines the infinitesimal deformation related to the gradient of the displacement $\frac{\partial u_i}{\partial x_j}$. ϵ_{ij} can be decomposed into normal (symmetric) and shear (asymmetric) components. The asymmetric contribution is carried by the tensor w_{ij}, defined as:

$$w_{ij} = \frac{1}{2}\left(\frac{\partial u_i}{\partial x_j} - \frac{\partial u_j}{\partial x_i}\right) \tag{A.4}$$

Appendix B

Convolution

A crystal is a periodic array of structural units such as atoms or molecules. It can be constructed by the infinite or unit cells or the basis. This is relevant to a convolution operation, one of the most important concepts in Fourier Theory. Mathematically, a convolution is defined as the integral over all space of one function $f(x)$ at a position x' multiplied by another function $g(x)$, reversed and shifted, at $(x - x')$. The convolution, denoted by $\otimes$ is defined as

$$(f \otimes g)(x) = \int_{-\infty}^{+\infty} f(x')g(x - x')\,\mathrm{d}x \tag{B.1}$$

The convolution is very useful until it has been applied to the Fourier transform. It can be expressed in two different ways:

The Fourier transform of a convolution is the product of the Fourier transforms.

$$\mathcal{F}(f \cdot g) = \mathcal{F}(f) \otimes \mathcal{F}(g); \tag{B.2}$$

The Fourier transform of a product is the convolution of the Fourier transforms.

$$\mathcal{F}(f \otimes g) = \mathcal{F}(f) \cdot \mathcal{F}(g) \tag{B.3}$$

According to the above equations, the convolution of two functions is equivalent to the multiplication of the Fourier transforms of the two functions, and vice versa. For example, when the Fourier transform is applied on time domain signals to obtain frequency spectra, the convolution of the original time domain signals is equal to multiplying the two frequency spectra. This is shown in the following equation:

$$f(t) \otimes g(t) = \mathcal{F}(f(t)) \cdot \mathcal{F}(g(t)) = F(w) \cdot G(w) \tag{B.4}$$

Appendix C

Undulator radiation

The emission angle θ is assumed to be 0 in equation (2.30). It can be extended to a general case (i.e. $\theta \neq 0$). The Doppler effect varies with the emission angle θ. The correct Doppler multiplication factor is $\gamma(1-\beta cos\theta)$. Assuming small angles $\beta \approx 1$ and take $cos\theta = 1 - \frac{\theta^2}{2} + ...$

$$f = \frac{c}{L(1-\beta cos\theta)} \tag{C.1}$$

$$f = \frac{c/L}{1-\beta(1-\theta^2/2+...)} = \frac{c/L}{1-\beta+\beta\theta^2/2-} = \frac{c/(1-\beta)L}{1+\beta\theta^2/2(1-\beta)...} \tag{C.2}$$

$$f = \frac{2\gamma^2 c/L}{1+\gamma^2\theta^2} = \frac{2\gamma^2 c}{L(1+\gamma^2\theta^2)} \tag{C.3}$$

The observed wavelength is then

$$\lambda = \frac{L}{2\gamma^2}(1 + \gamma^2\theta^2) \tag{C.4}$$

An electron passing through an undulator with N periods produces a wave train with N oscillations. For the first harmonic:

$$\frac{\Delta\lambda}{\lambda} = \frac{1}{N} \tag{C.5}$$

Write the wavelength twice, one for off-axis ($\theta \neq 0$), and one for on-axis radiation ($\theta = 0$).

$$\frac{\Delta\lambda}{\lambda} = \frac{\lambda(1 + \gamma^2\theta^2) - \lambda}{\lambda} = \gamma^2\theta^2 \tag{C.6}$$

Combining two equation (C.5) and (C.6):

$$\theta \approx \frac{1}{\gamma\sqrt{N}} \tag{C.7}$$

This is the half-angle of the central radiation cone, defined as containing radiation of $\Delta\lambda/\lambda = 1/N$.

Bibliography

[1] Y. C. Cao, R. Jin, and C. A. Mirkin, "Nanoparticles with raman spectroscopic fingerprints for dna and rna detection," *Science*, vol. 297, pp. 1536–1540, 2002.

[2] X. Huang, I. H. El-Sayed, W. Qian, and M. A. El-Sayed, "Cancer cell imaging and photothermal therapy in the near-infrared region by using gold nanorods," *J. Am. Chem. Soc.*, vol. 128, pp. 2115–2120, 2006.

[3] C.-Z. Li, K. B. Male, S. Hrapovic, and J. H. T. Luong, "Fluorescence properties of gold nanorods and their application for dna biosensing," *Chem. Commun.*, vol. 31, pp. 3924–3926, 2005.

[4] P. K. Sudeep, S. T. S. Joseph, and K. G. Thomas, "Selective detection of cysteine and glutathione using gold nanorods," *J. Am. Chem. Soc.*, vol. 127, pp. 6516–6517, 2005.

[5] G. J. Williams, M. A. Pfeifer, I. A. Vartanyants, and I. K. Robinson, "Three-dimensional imaging of microstructure in au nanocrystals," *Phys. Rev. Lett.*, vol. 90, pp. 175 501–175 504, 2003.

[6] M. A. Pfeifer, G. J. Williams, I. A. Vartanyants, R. Harder, and I. K. Robinson, "Three-dimensional mapping of a deformation field inside a nanocrystal," *Nature*, vol. 442, pp. 63–66, 2006.

[7] I. K. Robinson and R. Harder, "Coherent x-ray diffraction imaging of strain at the nanoscale," *Nat. Mater.*, vol. 8, pp. 291–298, 2009.

[8] A. Ulvestad, H. M. Cho, R. Harder, J. W. Kim, S. H. Dietze, E. Fohtung, Y. S. Meng, and O. G. Shpyrko, "Nanoscale strain mapping in battery nanostructures," *Appl. Phys. Lett.*, vol. 104, pp. 073 108–073 112, 2014.

[9] A. Singer, A. Ulvestad, H. M. Cho, J. W. Kim, J. Maser, R. Harder, Y. S. Meng, and O. G. Shpyrko, "Nonequilibrium structural dynamics of nanoparticles in $LiNi_{1/2}Mn_{3/2}O_4$ cathode under operando conditions," *Nano Lett.*, vol. 14, pp. 5295–5300, 2014.

[10] A. Ulvestad, A. Singer, H. M. Cho, J. N. Clark, R. Harder, J. Maser, Y. S. Meng, and O. G. Shpyrko, "Single particle nanomechanics in operando batteries via lensless strain mapping," *Nano Lett.*, vol. 14, p. 51235127, 2014.

[11] X. Huang, R. Harder, S. Leake, J. Clark, and I. Robinson, "Three-dimensional bragg coherent diffraction imaging of an extended zno crystal," *J. Appl. Cryst.*, vol. 45, pp. 778–784, 2012.

[12] J. Kim, S. Manna, S. Manna, S. Dietze, A. Ulvestad, R. Harder, E. Fohtung, E. Fullerton, and O. Shpyrko, "Curvature-induced and thermal strain in polyhedral gold nanocrystals," *Appl. Phys. Lett.*, vol. 105, pp. 173 108–173 112, 2014.

[13] J. Miao, P. Charalambous, J. Kirz, and D. Sayre, "Extending the methodology of x-ray crystallography to allow imaging of micrometre-sized non-crystalline specimens," *Nature*, vol. 400, pp. 342–344, 1999.

[14] B. E. Warren, "X-ray diffraction," *Dover Publ. Inc., New York*, pp. 2173–2186, 1990.

[15] J. Als-Nielsen and D. McMorrow, "Elements of modern x-ray physics," *John Wiley and Sons, New York*, 2011.

[16] I. A. Vartanyants and I. K. Robinson, "Partial coherence effects on the imaging of small crystals using coherent x-ray diffraction," *J. Phys.: Condens. Matter*, vol. 13, pp. 10 593–10 611, 2001.

[17] S. J. Leake, M. C. Newton, R. Harder, and I. K. Robinson, "Longitudinal coherence function in x-ray imaging of crystals," *Optics Express*, vol. 17, pp. 15 853–15 859, 2009.

[18] L. Mandel and E. Wolf, "Optical coherence and quantum optics," *Cambridge University Press*, 1995.

[19] D. H. Bilderback, P. Elleaume, and E. Weckert, "Review of third and next generation synchrotron light sources," *J. Phys. B: At. Mol. Opt. Phys.*, vol. 38, pp. 773–797, 2005.

[20] E. Beaurepaire, H. Bulou, F. Scheurer, and J. Kappler, "Magnetism and synchrotron radiation," *Springer proceedings in physics*, vol. 133, pp. 127–144, 2010.

[21] G. Margaritondo, "A primer in synchrotron radiation: Everything you wanted to know about synchrotron emission of x-rays but were afraid to ask," *J. Synchrotron Rad.*, vol. 2, pp. 148–154, 1995.

[22] D. M. Mills, J. R. Helliowell, A. Kvick, T. Ohta, I. Robinson, and A. Authier, "Report of the working group on synchrotron radiation nomenclature brightness, spectral brightness or brilliance," *J. Synchrotron Rad.*, vol. 12, p. 385, 2005.

[23] L. Beitra, M. Watari, T. Matsuura, N. Shimamoto, R. Harder, and I. Robinson, "Confocal microscope alignment of nanocrystals for coherent diffraction imaging," *The10th international conference on synchrotron radiation instrumentation.*

[24] S. J. Leake, M. C. Newton, R. Harder, and I. K. Robinson, "Coherence function in x-ray imaging of crystals," *Optics Express*, vol. 17, pp. 15 853–15 859, 2009.

[25] L. Beitra, M. Watari, T. Matsuura, N. Shimamoto, R. Harder, and I. Robinsona, "Confocal microscope alignment of nanocrystals for coherent diffraction imaging," *AIP Conference Proceedings*, vol. 1234, pp. 57–60, 2010.

[26] J. Miao, J. Kirz, and D. Sayre, "The oversampling phasing method," *Acta Crystallogr. Sect. D: Biol. Crystallogr.*, vol. 56, pp. 1312–1315, 2000.

[27] J. Miao, P. Charalambous, J. Kirz, and D. Sayre, "Extending the methodology of x-ray crystallography to allow imaging of micrometre-sized non-crystalline specimens," *Nature*, vol. 400, pp. 342–344, 1999.

[28] C. Shannon, "Communication in the presence of noise," *Proc. Inst. Radio Eng.*, vol. 37, pp. 10–21, 1949.

[29] D. Sayre, "Some implications of a theorem due to shannon," *Acta Crystallogr.*, vol. 5, pp. 843–21, 1952.

[30] J. Miao, D. Sayre, Chapman, and H. N, "Confocal microscope alignment of nanocrystals for coherent diffraction imaging," *J. Opt. Soc. Am.*, vol. 15, pp. 1662–1669, 1998.

[31] R. W. Gerchberg and W. O. Saxton, "A practical algorithm for the determination of the phase from image and diffraction plane pictures," *Optik (Jena)*, vol. 35, pp. 237–246, 1972.

[32] J. R. Fienup, "Phase retrieval algorithms: a comparison," *Appl. Opt.*, vol. 21, pp. 2758–2769, 1982.

[33] J. R. Fienup and C. C. Wackerman, "Phase-retrieval stagnation problems and solutions," *J. Opt. Soc. Am. A*, vol. 3, pp. 1897–1907, 1986.

[34] J. Fienup, "Reconstruction of a complex-valued object from the modulus of its fourier transform using a support constraint," *J. Opt. Soc. Am. A*, vol. 4, pp. 118–123, 1986.

[35] R. P. Millane and W. J. Stroud, "Reconstructing symmetric images from their under-sampled fourier intensities," *J. Opt. Soc. Am. A*, vol. 14, pp. 568–579, 1997.

[36] J. P. Abrahams and A. G. W. Leslie, "Methods used in the structure determination of bovine mitochondrial f1 atpase," *Acta. Crystallography D*, vol. 52, pp. 30–42, 1996.

[37] V. Elser, "Phase retrieval by iterated projections," *J. Opt. Soc. Am.*, vol. 20, pp. 40–55, 2003.

[38] H. H. Bauschke, P. L. Combettes, and D. R. Luke, "Phase retrieval, error reduction algorithm, and fienup variants: a view from convex optimization," *J. Opt. Soc. Am. A*, vol. 19, pp. 1334–1345, 2002.

[39] H. H. Bauschke, P. L. Combettes, and D. Luke, "Hybrid projection reflection method for phase retrieval," *J. Opt. Soc. Am.*, vol. 20, pp. 1025–1034, 2003.

[40] D. R. Luke, "Relaxed averaged alternating reflections for diffraction imaging," *Inverse Problems*, vol. 21, pp. 37–50, 2005.

[41] S. Marchesini, H. He, H. N. Chapman, S. P. Hau-Riege, A. Noy, M. R. Howells, U. Weierstall, and J. C. H. Spence, "X-ray image reconstruction from a diffraction pattern alone," *Phys. Rev. B*, vol. 68, pp. 140 101–140 104, 2003.

[42] M. D. Graef and M. E. McHenry, "Structure of materials," *Cambridge University Press*, p. 159, 2007.

[43] C. Herring, *Angew. Chem.*, vol. 65, p. 34, 1953.

[44] G. Wulff, "Zur frage der geschwindigkeit des wachstums und der auflosung von krystallflachen," *Z. Kristallogr.*, vol. 34, pp. 449–530, 1901.

[45] H. Lüth, "Surfaces and interfaces of solid," *Springer*, 1993.

[46] T. Young, "Cohesion of fluids," *Phil. Trans.*, p. 65, 1805.

[47] J. Sheng, U. Welzel, and E. J. Mittemeijer, "Nonmonotonic crystallite-size dependence of the lattice parameter of nanocrystalline nickel," *Appl. Phys. Lett.*, vol. 97, pp. 153 109–153 111, 2010.

[48] W. Haiss, "Surface stress of clean and adsorbate-covered solids," *Rep. Prog. Phys.*, vol. 64, pp. 591–648, 2001.

[49] H. Ibach, "The role of surface stress in reconstruction, epitaxial growth and stabilization of mesoscopic structures," *Surf. Sci. Rep.*, vol. 29, pp. 195–263, 1997.

[50] E. P. Murray, T. Tsai, and S. A. Barnett, "A direct-methane fuel cell with a ceria-based anode," *Nature*, vol. 400, pp. 649–651, 1999.

[51] K. T. Chan, J. J. Kan, C. Doran, L. Ouyang, D. J. Smith, and E. E. Fullerton, "Controlled growth behavior of chemical vapor deposited ni nanostructures," *Philosophical Magazine*, vol. 92, pp. 2173–2186, 2012.

[52] K. T. Chan, J. J. Kan, C. Doran, L. Ouyang, D. J. Smith, , and E. E. Fullerton, "Oriented growth of single-crystal ni nanowires onto amorphous sio2," *Nano Lett.*, vol. 10, pp. 5070–5075, 2010.

[53] W. J. Huang, R. Sun, J. Tao, L. D. Menard, R. G. Nuzzo, and J. M. Zuo, "Coordination-dependent surface atomic contraction in nanocrystals revealed by coherent diffraction," *Nat. Mater.*, vol. 7, pp. 308–313, 2008.

[54] S. K. Ghosh and T. Pal, "Interparticle coupling effect on the surface plasmon resonance of gold nanoparticles: From theory to applications," *Chem. Rev.*, vol. 107, pp. 4797–4862, 2007.

[55] K. L. Kelly, E. Coronado, L. L. Zhao, and G. C. Schatz, "The optical properties of metal nanoparticles: The influence of size, shape, and dielectric environment," *J. Phys. Chem. B*, vol. 107, pp. 668–677, 2003.

[56] X. Qian and H. S. Park, "The influence of mechanical strain on the optical properties of spherical gold nanoparticles," *J. Mech. Phys. Solids*, vol. 58, pp. 330–345, 2010.

[57] L. D. Marks, "Experimental studies of small particle structures," *Rep. Prog. Phys.*, vol. 57, pp. 603–649, 1994.

[58] Z. L. Wang, "Transmission electron microscopy of shape-controlled nanocrystals and their assemblies," *J. Phys. Chem. B.*, vol. 104, pp. 1153–1175, 2000.

[59] S. Takagi, "A dynamical theory of diffraction for a distorted crystal," *J. Phys. Soc. Jpn*, vol. 26, pp. 1239–1253, 1969.

[60] J. R. Fienup, J. C. Marron, T. J. Schulz, and J. H. Seldin, "Hubble space telescope characterized by using phase-retrieval algorithms," *Appl. Opt.*, vol. 32, pp. 1747–1767, 1993.

[61] F. W. Smith and G. Ghidini, "Reaction of oxygen with si(111) and (100): Critical conditions for the growth of sio_2," *J. Electrochem. Soc.*, vol. 129, pp. 1300–1306, 1982.

[62] C. J. Murphy, A. M. Gole, S. E. Hunyadi, and C. J. Orendorff, "One-dimensional colloidal gold and silver nanostructures," *Inorg. Chem.*, vol. 45, pp. 7544–7554, 2006.

[63] C. Ni, P. A. Hassan, and E. W. Kaler, "Structural characteristics and growth of pentagonal silver nanorods prepared by a surfactant method," *Langmuir*, vol. 21, pp. 3334–3337, 2005.

[64] S. H. Kim, B. S. Choi, K. Kang, Y. S. Choi, and S. I. Yang, "Low temperature synthesis and growth mechanism of ag nanowires," *J. Alloys Compd.*, vol. 433, pp. 261– 264, 2007.

[65] X. Zhang, "Controlling synthesis of silver nanowires and dendrites in mixed surfactant solutions," *J. Colloid Interface Sci.*, vol. 268, pp. 357– 361, 2003.

[66] I. A. Vartanyants and I. K. Robinson, "Partial coherence effects on the imaging of small crystals using coherent x-ray diffraction," *J. Phys.: Condens. Matter*, vol. 13, pp. 10 593–10 611, 2001.

[67] V. Germain, J. Li, D. Ingert, Z. L. Wang, and M. P. Pileni, "Stacking faults in formation of silver nanodisks," *J. Phys. Chem. B*, vol. 107, pp. 8717–8720, 2003.

[68] C. Lofton and W. Sigmund, "Mechanisms controlling crystal habits of gold and silver colloids," *Adv. Funct. Mater.*, vol. 15, pp. 1197–1208, 2005.

[69] Y. Sun and C. An, "Shaped gold and silver nanoparticles," *Front. Mater. Sci.*, vol. 5, pp. 1–24, 2011.

[70] M. Watari, R. McKendry, M. Voegtli, G. Aeppli, Y.-A. Soh, X. Shi, G. Xiong, X. Huang, R. Harder, and I. K. Robinson, "Differential stress induced by thiol adsorption on facetted nanocrystals," *Nat. Mater.*, vol. 10, pp. 862–866, 2011.

[71] I. K. Robinson, "Nanoparticle structure by coherent x-ray diffraction," *J. Phys. Soc. Jpn.*, vol. 82, pp. 021 012–021 018, 2013.

[72] B. Gilbert, F. Huang, H. Zhang, G. A. Waychunas, and J. F. Banfield, "Nanoparticles: Strained and stiff," *Science*, vol. 305, pp. 651–654, 2004.

[73] F. Ruffino, C. Bongiorno, F. Giannazzo, F. Roccaforte, V. Raineri, and M. G. Grimaldi, "Effect of surrounding environment on atomic structure and equilibrium shape of growing nanocrystals," *Nanoscale. Res. Lett.*, vol. 2, pp. 240–247, 2007.

[74] D. Y. Kim, S. H. Im, and O. O. Park, "Evolution of gold nanoparticles through catalan, archimedean, and platonic solids," *CrystEngComm*, vol. 12, pp. 116–121, 2010.

[75] C. Liang, S. Huang, W. Zhao, W. Liu, J. Chen, H. Liu, and Y. Tong, "Polyhedral Fe_3O_4 nanoparticles for lithium ion storage," *New J. Chem.*, 2015.

[76] S. Boutet and I. Robinson, "Coherent x-ray diffractive imaging of protein crystals," *J. Synchrotron Rad.*, vol. 13, pp. 1–8, 2006.

[77] M. R. Howells, A. Hitchcock, and C. J. Jacobsen, "Introduction: Special issue on radiation damage," *J. Electron Spectrosc. Relat. Phenom.*, vol. 170, pp. 1–3, 2009.

[78] T. Schafer, P. Michel, F. Claret, T. Beetz, S. Wirick, and C. Jacobsen, "Radiation sensitivity of natural organic matter: Clay mineral association effects in the callovo-oxfordian argillite," *J. Electron Spectrosc. Relat. Phenom.*, vol. 170, pp. 49–56, 2009.

[79] M. R. Howells, T. Beetz, H. N. Chapman, C. Cui, J. M. Holton, C. J. Jacobsen, E. L. J. Kirz, S. Marchesini, H. Miao, D. Sayre, D. A. Shapiro, J. C. H. Spence, and D. Starodub, "An assessment of the resolution limitation due to radiation-damage in x-ray diffraction microscopy," *J. Electron Spectrosc. Relat. Phenom.*, vol. 170, pp. 4–12, 2009.

[80] Y. C. Sasaki, Y. Okumura, T. Miyazaki, T. Higurashi, and N. Oishi, "Observations of x-ray radiation pressure force on individual gold nanocrystals," *Appl. Phys. Lett.*, vol. 89, pp. 053 121–053 123, 2006.

[81] V. Chamard, J. Stangl, G. Carbone, A. Diaz, G. Chen, C. Alfonso, C. Mocuta, and T. H. Metzger, "Three-dimensional x-ray fourier transform holography: The bragg case," *Phys. Rev. Lett.*, vol. 104, pp. 165 501–165 504, 2010.

[82] X. Shi, G. Xiong, X. Huang, R. Harder, and I. Robinson, "Radiation-induced bending of silicon-on-insulator nanowires probed by coherent x-ray diffractive imaging," *New J. Phys.*, vol. 14, pp. 063 029–063 031, 2012.

[83] P. Debye, "X-ray interference and thermal movement," *Ann. Physik,*, vol. 43, p. 49, 1914.

[84] S. Hoffmann, I. Utke, B. Moser, J. Michler, S. H. Christiansen, V. Schmidt, S. Senz, P. Werner, U. Gsele, and C. Ballif, "Measurement of the bending strength of vapor-liquid-solid grown silicon nanowires," *Nano Letters*, vol. 6, pp. 622–625, 2006.